TECHNISCHE UNIVERSITÄT DRESDEN

Study of EFT effects on the electroweak quartic $WW\gamma\gamma$ vertex in $\gamma\gamma jj$ Production

Bachelorarbeit
zur Erlangung des Hochschulgrades
Bachelor of Science
im Bachelor-Studiengang Physik

vorgelegt von

Justin Gründling
geboren am 09.01.2001 in Eilenburg

Institut für Kern- und Teilchenphysik
Fakultät Physik
Bereich Mathematik und Naturwissenschaften
Technische Universität Dresden

23.01.2024

Eingereicht am 23. Januar 2024

1. Gutachter: Dr. Frank Siegert
2. Gutachter: Prof. Dr. Dominik Stöckinger

Abstract

In high energy physics, it is very interesting to study the scattering of vector bosons, as these processes are very rare and could be used to get more insight into the electroweak symmetry breaking and confirm the Standard Model or even discover physics beyond the Standard Model. One possibility to quantify physics beyond the Standard Model are effective field theories (EFTs), which introduce new interactions or modify existing ones. These EFTs use so-called Wilson coefficients as a parameter that characterizes the coupling strength of the added interaction. For these coefficients only lower and upper limits have been found. This thesis focuses on testing the agreement of the current limits of dim-8 EFT operators with the Standard Model using Monte Carlo simulations. This is done for the process of $WW\gamma\gamma$ vector boson scattering, by visually comparing the data for kinematic observables of the EFT operators and the Standard Model. All this is done considering the technical limitations of the ATLAS detector and LHC for the time of run 2 and a simple analysis of uncertainties.

Zusammenfassung

In der Hochenergiephysik ist es sehr interessant, die Streuung von Vektorbosonen zu untersuchen, da diese Prozesse sehr selten sind und genutzt werden könnten, um mehr Einblick in die elektroschwache Symmetriebrechung zu erhalten und das Standardmodell zu bestätigen oder sogar Physik jenseits des Standardmodells zu entdecken. Eine Möglichkeit, Physik jenseits des Standardmodells zu quantifizieren, sind effektive Feldtheorien (EFTs), die neue Wechselwirkungen einführen oder bestehende modifizieren. Diese EFTs verwenden so genannte Wilson-Koeffizienten als Parameter, der die Kopplungsstärke der zusätzlichen Wechselwirkung charakterisiert. Für diese Koeffizienten wurden bisher nur untere und obere Grenzwerte gefunden. Diese Arbeit konzentriert sich darauf, die Übereinstimmung der aktuellen Grenzen der dim-8 EFT-Operatoren mit dem Standardmodell mit Hilfe von Monte-Carlo-Simulationen zu testen. Dies geschieht für den Prozess der $WW\gamma\gamma$-Vektorbosonenstreuung, indem die Daten für kinematische Observablen der EFT-Operatoren und des Standardmodells visuell verglichen werden. All dies geschieht unter Berücksichtigung der technischen Beschränkungen des ATLAS-Detektors und des LHC für die Zeit von Lauf 2 und einer einfachen Analyse der Unsicherheiten.

Contents

1 Introduction **1**

2 Theoretical and Experimental Foundation **3**

2.1 The Large Hadron Collider and ATLAS-Detector . . . 3

2.1.1 The Large Hadron Collider . . . 3

2.1.2 The ATLAS Detector . . . 4

2.2 The Standard Model of Particle Physics . . . 5

2.2.1 Quantum Chromodynamics . . . 7

2.2.2 Electroweak Interaction . . . 8

2.2.3 Spontaneous Symmetry Breaking . . . 9

2.3 Processes for $\gamma\gamma jj$ Production . . . 11

2.4 Extending the Standard Model . . . 13

2.4.1 Mathematical formulation of an EFT . . . 13

2.4.2 Operators . . . 14

2.4.3 Wilson Coefficients . . . 15

2.4.4 Decomposition . . . 16

3 Methods **17**

3.1 Event Generation . . . 17

3.2 Runcards . . . 17

3.3 Data Analysis . . . 20

4 Results **25**

5 Summary and Outlook **37**

A Appendix **45**

Acronyms and Conventions

SM	Standard Model
BSM	Beyond Standard Model
QFT	Quantum Field Theory
EFT	Effective Field Theory
VB	Vector Boson
VBS	Vector Boson Scattering
VBF	Vector Boson Fusion
QED	Quantum Electrodynamics
QFD	Quantum Flavourdynamics
EW	Electroweak
QCD	Quantum Chromodynamics
SSB	Spontaneous Symmetry Breaking
SUSY	Super-Symmetry
LO	Leading order
NLO	Next to leading order
CERN	European Organisation for Nuclear Research
LHC	Large Hadron Collider
MC	Monte Carlo
ME	Matrix Element
CL	Confidence Level

1 Introduction

The Standard Model (SM) of particle physics is currently the best theory to describe the observed particles and interactions that form reality. However the SM is not able to explain every phenomenon observed in nature, for example it does not incorporate gravity, Baryon asymmetry, dark matter or the mass of neutrinos. To find a complete theory, modern particle physicists test the limits of the SM in particle accelerators like the Large Hadron Collider (LHC). It accelerates protons to close to the speed of light and collides them resulting in all kinds of processes, the products of which are then measured in particle detectors like ATLAS. These high energy collisions make it possible to observe rare processes, because the allow for the production of particles, the coupling of which is comparatively weak, but rises with the particles energy. An example of these rare processes are the self interactions of electroweak gauge bosons, which are very unlikely to happen even in these energy regimes due to the high masses of the participants and the comparatively weak coupling of the electroweak interaction. Nevertheless these processes are interesting to study due to their connection to the electroweak symmetry breaking. Because of this, they might provide more insight into the limitations of the SM in the form of deviations, which could indicate physics beyond the Standard Model (BSM). This this thesis focuses on the quartic interaction of two W bosons and two photons (fig.1.1), which is predicted by the electroweak interaction within the SM. This process will be

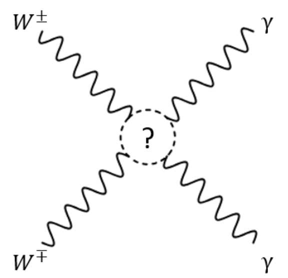

Figure 1.1: $WW\gamma\gamma$ vertex

studied by simulating it using the Monte Carlo (MC) event generator Sherpa [1], within the boundaries of the SM comparing it to simulations where these boundaries are expanded with a so-called effective field theory (EFT). These are a way to quantify BSM physics without knowledge of the underlying theory. To compare these simulations to actual data from the ATLAS detector in a future study, the simulations are performed at a center of mass energy of $\sqrt{s} = 13\,\mathrm{TeV}$ and an integrated luminosity of $L = 139\,\mathrm{fb}^{-1}$. Those parameters correspond to the data taking period of ATLAS in LHC run 2. This thesis presents a visual comparison of the EFT effects, within currently known limits, and the SM predictions for the differential cross section of this process. This is done to determine if the EFT limits [2] of the studied operators, could be improved with this process, or whether the current technical limitations do not allow for such improvements.

2 Theoretical and Experimental Foundation

2.1 The Large Hadron Collider and ATLAS-Detector

To compare the later simulated data to real, measured data, the settings of the simulation will be set to the parameters of the Large Hadron Collider (LHC) run 2. Since the event selection should be according to the limitations of the ATLAS detector, these are implemented in the analysis of the data, to allow for comparisons. The first Run of the LHC from 2010 to 2013 had a beam energy of about $4\,\mathrm{TeV}$ was resulting in a center-of-mass energy of $\sqrt{s} = 8\,\mathrm{TeV}$, multiple times the previous world record. In the second run [3] from 2015 to 2018, this was already improved to a beam energy of $\sqrt{s} = 6.5\,\mathrm{TeV}$ per beam, so a center of mass energy of $13\,\mathrm{TeV}$. At the time of this thesis, the LHC is in run 3, where the center of mass energy was again increased, reaching $\sqrt{s} = 14\,\mathrm{TeV}$ and an integrated luminosity of $300\,\mathrm{fb}^{-1}$ is aimed for [4]. Since the data taking of run 3 is not planned to be finished until 2025 and the data analysis taking some additional years, here the technical specifications of LHC and ATLAS for run 2 are used, so a comparison between the simulated data and real experimental data would be possible.

2.1.1 The Large Hadron Collider

The LHC [5] is a particle collider located at CERN, near Genf, in Switzerland, built with the goal of finding new particles and phenomena. It is currently the world's largest and most powerful collider, with a circumference of 27 kilometres. It's operation began in 2008. In 2012 the ATLAS collaboration published their most significant study, the discovery of the Higgs boson [6]. In the LHC mainly proton beams, but also lead ions, are accelerated to close of the speed of light and brought to collision. To achieve the collision an extremely high precision beam has to be created. to increase the probability of the collision, the photons travel in bunches of about $1.15 \cdot 10^{11}$ particles, yet per bunch crossing only about 2800 collisions happen. But since the bunch collision rate is about $40\,\mathrm{MHz}$, the amount of data produced is to high to keep for all events. Because of this, triggers are implemented that filter the events in real time, scrapping more than 99% of the produced event data, since it does not provide clear insight into the underlying processes. For run 2 a center of mass energy of $\sqrt{s} = 13\,\mathrm{TeV}$

was achieved. These high energies are achieved by guiding the beams through the circular tube, in opposite direction, within a ultrahigh vacuum. The guiding of the beams is done by superconductor electromagnets along the tube. The quantity physicists are interested in, is the differential cross section of a process, since this is directly proportional to the probability of a process happening within a certain phase space region. To obtain a high number events N, and therefor a statistical significant differential cross section, a high luminosity is needed, which is proportional to the number of collisions in the detectors. With the luminosity, the number of events and with that, the processes cross section can be calculated. It is differentiated between instantaneous $\mathcal{L}(t)$ and integrated luminosity L. The process cross section luminosity and number of events are connected according to:

$$\frac{dN}{dt} = \mathcal{L}(t) \cdot \sigma \implies N = \sigma \int \mathcal{L}(t) dt = \sigma \cdot L. \tag{2.1}$$

For the LHC run 2 an integrated luminosity of $L = 139\,\mathrm{fb}^{-1}$ [7] was calculated. This can be used to calculate the expected number of signal events for a given process from a simulated cross section.

2.1.2 The ATLAS Detector

At the collision points of the LHC, multiple detectors are built for different kinds of measurements. One of those is the ATLAS [8] detector, which is also currently the largest detector in the world [9]. The momentum of particles with electromagnetic charge is measured in the

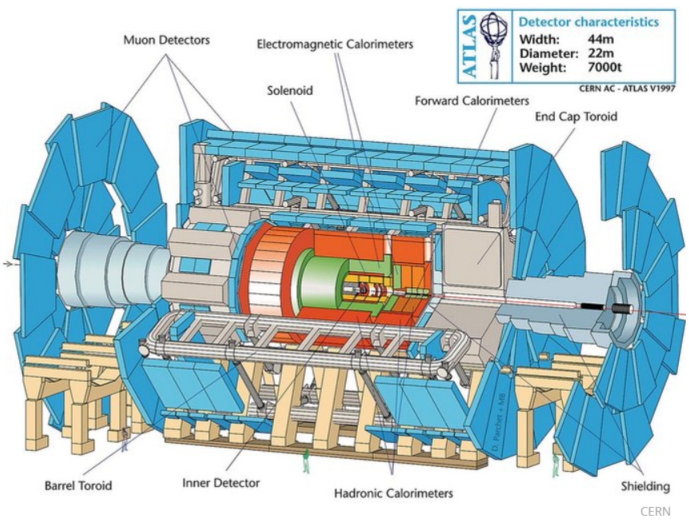

Figure 2.1: Structure of the ATLAS detector. Graphic taken from: [10]

inner detector, which is embedded in strong electromagnetic fields, which divert them. The particle's charge and momentum are then computed via the measurement of the trace radius. Most information is obtained from the induced electromagnetic and hadronic showers, produced by photons or electrons and hadrons respectively. Photons are detected within the electromagnetic calorimeter. The photon's interaction with high density lead plates leads to the production of electron-positron pairs which can then induce new photons in the liquid argon scintillator layers. This calorimeter is accordion shaped, to achieve uniform segmentation over the azimuthal plane and has a pseudorapidity coverage of $|\eta| < 4.9$, which is equal to an angle of about 89°, meaning only < 1° in the forward region is not covered. The hadronic calorimeter works in a similar way, here the absorber-medium is steel and a plastic scintillator is used. It is extended by the Hadronic End-Cap Calorimeter (HEC) and the Forward Calorimeter (FCal), which are Cu+lAr / Cu-W+lAr detectors, extending this calorimeters coverage of pseudorapidity to also $|\eta| < 4.9$. Here particle production mostly happens via the strong interaction. The measured, quantities, including the deposited energy can then be used to reconstruct the original particle. The particles need a certain minimum momentum to induce the showers. Additionally to the mentioned parts, there are more, such as the muon chamber, where muons can be measured. But since these particles do not appear in the final state of the processes this thesis focuses on, these will not be further explained. The coordinate system of the detector is build using the azimuthal angle in the transverse plane ϕ, the pseudorapidity $\eta = -ln\big(tan\big(\frac{\theta}{2}\big)\big) = \frac{1}{2}ln\big(\frac{|\vec{p}|+p_z}{|\vec{p}|-p_z}\big)$, which directly relates to the polar angle relative to the beam axis θ and p_z the momentum component parallel to the beam axis. Additionally, commonly used observables are the transverse momentum p_T, so the momentum component perpendicular to the beam axis, the particle energy deposited in the calorimeter system E, the rapidity $Y = \frac{1}{2}ln\big(\frac{E+p_z}{E-p_z}\big)$ and the angular distance $\Delta R_{ij} = \sqrt{(\Delta\eta_{ij})^2 + (\Delta\phi_{ij})^2}$. With these equations it also becomes clear, that for $|p| \to E$, the rapidity and pseudorapidity of a particle approach one another, as the particles masses can be neglected, and for massless particles, they are equal.

2.2 The Standard Model of Particle Physics

In this section, a brief introduction to the Standard Model of particle physics is provided, based on the explanations in [11, 12]. The SM is currently the best tested fundamental theory of microscopic interactions, and describes most observed phenomena in particle physics. It is a renormalizable UV-complete quantum field theory (QFT), which means it is a QFT that preserves unitarity at all energy scales. The theory consists of three different interactions, namely the electromagnetic, the weak , and the strong interaction, described by Quantum Electrodynamics (QED), Quantum Flavourdynamics (QFD) and Quantum Chromodynamics (QCD), respectively. Later it was found, that the QED and QFD can be unified into one interaction, called electroweak (EW) interaction. It is formulated as a Yang-Mills-theory [13], meaning a gauge theory, which can be based on any compact Lee-group. In the case of the SM, the SU(n) group is used. A gauge theory assumes gauge symmetry of the local phase of a particle, so invariance under a transformation of the kind:

$$\psi \rightarrow e^{i\varphi(x)}\psi. \tag{2.2}$$

The full symmetry group of the theory, which leads to the different particles and interactions is the non-abelian $SU(3)_C \otimes SU(2)_L \otimes U(1)_Y$, where the $SU(3)_C$ leads to the strong interaction and $SU(2)_L \otimes U(1)_Y$ to the EW interaction. The Standard Model predicts a number fermions, which are the particles that we perceive as matter and which bear a spin of $s = \frac{1}{2}$, and bosons, which are the carriers of the interaction and have an integer spin $s = 0, 1$. The gauge bosons

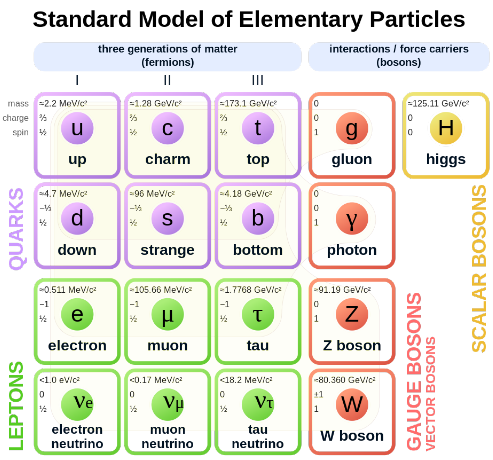

Figure 2.2: Particles described by the SM. Graphic taken from: [14]

of each interaction in the Standard Model only couple to particles that carry the respective interaction charge of the boson. The photon for example only couples to electrically charged particles, and since they themselves are not electrically charged, there is no self interaction between the photons. In the QCD the gauge bosons, called gluons, carry a color charge themselves, which leads to self interaction between them.

Though the SM is currently our best description of reality, it is known to be incomplete, since it fails to unify the known quantum interactions with gravity as described by the general theory of relativity. Since the creation of the SM, many attempts have been made to find theories to extend it and create a Grand Unified Theory (GUT), e.g. Super-Symmetry (SUSY) [15] but none of these theories have been confirmed by experiments yet. A more general possibility to extend the SM are effective field theories, which will be discussed in section 2.4.

2.2.1 Quantum Chromodynamics

Based on the QCD being a gauge theory, build on the $SU(3)$ symmetry group, the lagrange density is found to be:

$$\mathcal{L} = -\frac{1}{4}\sum_{a=1}^{8} F^{a\mu\nu}F^{a}_{\mu\nu} + \sum_{j=1}^{n_f} \bar{q}_j(i\not{D} - m_j)q_j. \tag{2.3}$$

Here the q_j are the different quark fields of n_f different flavours and masses m_j. The term between the quark fields is the Dirac equation, where $\not{D} = D_\mu\gamma^\nu$, with the Dirac matrices γ^μ and the covariant derivative:

$$D_\mu = \partial_\mu - ie_s\sum_a t^a g^a_\mu. \tag{2.4}$$

One can find e_s as the gauge coupling and $\alpha_s = \frac{e_s^2}{4\pi}$ as the coupling constant[1]. The g^a_μ refer to the eight gluon fields and the t^a are the generators of the $SU(3)$ group, written as 3×3 matrices that act on the quarks in triplet notation. In the first sum, one can see the gluon field strength tensor:

$$F^a_{\mu\nu} = \partial_\mu g^a_\nu - \partial_\nu g^a_\mu - e_s f_{abc} g^b_\mu g^c_\nu, \tag{2.5}$$

which is constructed with the four-derivatives of the gluon fields and an additional last term with the asymmetric structure constant f_{abc}, which leads to self interactions between the gluons.

The features that differentiate the QCD from classical forces are the The QCD has unique features, which distinguish it from other forces, such as asymptotic freedom and confinement [16]. In field theories the relevant coupling constants are not truly constant but depend on the interaction, more specifically the transferred four-momentum squared Q^2. In the case of QCD the relevant coupling is $\alpha_s(Q^2)$. Asymptotic freedom means, that α_s decreases as Q^2 increases, and vanishes asymptotically. Because of this, the interaction via QCD becomes relatively weak for large Q^2, so called hard processes, or deep inelastic scattering, as is the case in particle colliders like the LHC. Confinement on the other hand refers to the property of QCD, that the interaction at short distances behaves similar to the coulomb-potential $\sim \frac{\alpha_s(r)}{r}$, while at large distances the interaction strength rises exponentially. This results in the phenomenon, that particles with color charge always appear as overall color neutral systems. If the particles are separated far enough spatially, the interaction strength rises to a point where it costs less energy to create a new quark-antiquark pair, which again form a color neutral state of the system. For example consider a $e^+e^- \to \bar{q}q$ process. In a particle collider this would result in these two particles having large, oppositely directed momenta. Due to the confinement the large spatial separation would lead to the creation of new particle pairs between them, which makes it impossible to identify the original final state quarks. This process is measured as

[1] in natural units ($\hbar = c = 1$)

two colorless jets, which is a narrow cone of hadrons, going in opposite directions. Sometimes also a well identifiable third jet can be measured, which comes from a high energy gluon being emitted from the original quarks.

2.2.2 Electroweak Interaction

The electroweak (EW) interaction stems from the unification of QED and QFD. The lagrange density of the EW interaction can be split into two parts:

$$\mathcal{L}_{EW} = \mathcal{L}_{Int} + \mathcal{L}_{SSB}, \tag{2.6}$$

where $\mathcal{L}_{Int}$ refers to the interactions between the particles, and $\mathcal{L}_{SSB}$ which is introduced by the spontaneous symmetry breaking in the Higgs-mechanism, and explains the masses of the EW gauge bosons. In this section the first term is discussed, while in (2.2.3) the second term is discussed.

$$\mathcal{L}_{Int} = -\frac{1}{4}\sum_{a=1}^{3} F^a_{\mu\nu}F^{a\mu\nu} - \frac{1}{4}B_{\mu\nu}B^{\mu\nu} + \bar{\psi}_L i\gamma^\mu D_\mu \psi_L + \bar{\psi}_R i\gamma^\mu D_\mu \psi_R \tag{2.7}$$

Equation 2.7 shows the the Yang-Mills Lagrangian of the $SU(2)_L \otimes U(1)_Y$ symmetry group. $F^a_{\mu\nu}$ and $B_{\mu\nu}$ are the gauge antisymmetric field strength tensors constructed from the associated gauge fields B_μ of the $U(1)_Y$ and W^a_μ (a=1,2,3) of the $SU(2)_L$. The field strength tensors are constructed as follows:

$$B_{\mu\nu} = \partial_\mu B_\nu - \partial_\nu B_\mu \tag{2.8}$$
$$F^a_{\mu\nu} = \partial_\mu W^a_\nu - \partial_\nu W^a_\mu - g\epsilon_{abc}W^b_\mu W^c_\nu \tag{2.9}$$

ϵ_{abc} is the structure constant of the group, which is given by the commutator relations of the generators. Since $SU(2)_L$ is also the group of spin-symmetry transformations, the generators of the group are the Pauli-matrices and the structure constant is just the Levi-Civita-tensor. This is also the reason why the charge corresponding to the weak force ($SU(2)_L$) is called weak-isospin. The γ^μ and D_μ in eq. 2.7 refer to the Dirac matrices and covariant derivative. Interactions with fermions are described by the last two terms, where the ψ stand for a sum over all flavours of quarks and leptons, which are split into a left and a right handed component:

$$\psi_{L/R} = \frac{(1 \mp \gamma_5)}{2}\psi \quad \text{and} \quad \bar{\psi}_{L/R} = \bar{\psi}\frac{(1 \pm \gamma_5)}{2}. \tag{2.10}$$

This is done, because the EW theory is a chiral theory, which means that the left and right handed components interact differently wit the gauge bosons. This is already visible in the fact, that the left handed fermions exist as doublets of the different flavors of each generation (up-/down-like quark or electron/neutrino lepton), which allows for transformations between them (flavour-change). Right handed fermions exist only as singlets, meaning they cannot participate in flavor-changing interactions. The covariant derivative is constructed to obey the gauge symmetry:

$$D_\mu = \partial_\mu + ig_W \sum_{a=1}^{3} T^a W_\mu^a + ig_Y Y B_\mu. \tag{2.11}$$

Here the T^a refer to the generators of the $SU(2)$ and Y to the weak hypercharge as the generator for the $U(1)$. To obtain the electrical charge, the weak hypercharge and the third isospin component have to be combined as $Q = I_w^3 + Y$ (sometimes also with an additional factor 2). This is in units of e, the electric charge of a positron. The g_w and g_Y are the couplings of the respective groups. Experimental observations show, that the physical bosons of the EW interaction, meaning the mass eigenstates, are combinations of the interaction eigenstates, where:

$$W_\mu^\pm = \frac{1}{\sqrt{2}}(W_\mu^1 \mp iW_\mu^2) \tag{2.12}$$

are the charged W bosons, which couple via the weak coupling g_W. There are also two neutral bosons, the photon and the Z boson:

$$\begin{pmatrix} A_\mu \\ Z_\mu \end{pmatrix} = \begin{pmatrix} cos\theta_w & sin\theta_w \\ -sin\theta_w & cos\theta_w \end{pmatrix} \begin{pmatrix} B_\mu \\ W_\mu^3 \end{pmatrix}. \tag{2.13}$$

The coupling of left and right handed fermions to photons is observed to be equal and proportional to the electric charge e. The neutrino is observed to not couple to the photon at all. With this the couplings have the following relation:

$$g_W sin\theta_w = g_Y cos\theta_w = e \tag{2.14}$$

Also the coupling of the Z boson can be found as $g_Z = \frac{e}{sin\theta_w cos\theta_w}$. The θ_w is the the so-called Weinberg-angle, or weak mixing angle, which is one of the free parameters of the SM.

2.2.3 Spontaneous Symmetry Breaking

At this point no masses for either the fermions or bosons are explained by the SM. This was fixed by the Brout-Englert-Higgs-mechanims (often refered to only as Higgs-mechanism) [17, 18, 19]. The mass terms of the particles should be of the form:

$$\frac{1}{2}m_W^2 W_\mu^a W^{a\mu} + \frac{1}{2}m_B^2 B_\mu B^\mu \quad \text{for spin one gauge bosons} \tag{2.15}$$

$$m^2 \psi\bar{\psi} \quad \text{for spin 1/2 fermions} \tag{2.16}$$

but these terms would not be invariant under the EW gauge group. This was solved by introducing a new complex scalar field:

$$\Phi = \begin{pmatrix} \theta^2(x) + i\theta^1(x) \\ \frac{1}{\sqrt{2}}(v + H(x) + i\theta^3(x)) \end{pmatrix} \tag{2.17}$$

with a vacuum ground state $v = \langle 0|\Phi|0\rangle \neq 0$. The field Φ is constructed as a $SU(2)_L$ doublet with a $U(1)_Y$ hypercharge and is built with four degrees of freedom, the Higgs-field $H(x) \in \mathbb{R}$ and the three complex Goldstone-modes $\theta^i(x)$. From this a scalar field Lagrangian can be constructed:

$$\mathcal{L}_\Phi = (D^\mu\Phi)^\dagger(D_\mu\Phi) - V(\Phi), \tag{2.18}$$

with the covariant derivative in eq. 2.11. The potential can be explicitly written as:

$$V(\Phi) = \mu^2|\Phi|^2 + \lambda|\Phi|^4 \tag{2.19}$$

where for $\mu^2 < 0$ and $\lambda > 0$ the potential has degenerate minima with non-zero value. Now the symmetry of the field is broken spontaneously, while leaving the Lagrangian symmetric under $SU(2)_L \times U(1)_Y$. For this one value of the minima is arbitrarily chosen. Canonically it is chosen as:

$$\Phi_0 = \begin{pmatrix} 0 \\ \frac{1}{\sqrt{2}v} \end{pmatrix} = \begin{pmatrix} 0 \\ \frac{1}{\sqrt{2}}\sqrt{-\frac{\mu^2}{\lambda}} \end{pmatrix}. \tag{2.20}$$

Here the first entry, the electrically charged Φ_0^+ was chosen to be zero to leave the $U(1)_{QED}$ unbroken, though as mentioned above the values can be chosen arbitrarily and only result in different amounts of work to obtain the same results. This leads to massive weak gauge bosons and a massless photon.

$$m_W = v\frac{g_W}{2} \tag{2.21}$$

$$m_Z = \frac{m_W}{cos\theta_w} \tag{2.22}$$

Additionally this mechanism introduces terms for the interaction of scalar (s=0) Higgs bosons, with the massive gauge bosons, a mass term for the Higgs boson $m_H = \sqrt{2\lambda v^2} = \sqrt{2\mu^2}$, aswell as a term for Higgs boson self interaction. The values μ^2 and λ are free parameters of the SM, and can be related to v, which can also be related to the Fermi coupling constant G_F:

$$v = \frac{1}{\sqrt{\sqrt{2}G_F}} \approx 246\,\mathrm{GeV} \tag{2.23}$$

To now also include fermion masses, another term in in the lagrangian is build, introducing the Yukawa couplings y_i^f.

$$\mathcal{L}_{ferm} = y_1^f \bar{\psi}_L^f \Phi \psi_R^f + y_2^f \bar{\psi}_L^f \Phi^c \psi_R^f + h.c. \tag{2.24}$$

The first term produces the masses for the charged leptons and down-type quarks, while the second term generates the masses of the up-type quarks, with the charge conjugate $\Phi^c = i\sigma_2\Phi^*$. Neutrinos masses are generally not described by the SM and they were originally thought to be massless. Their masses remain an active field of research until today.

2.3 Processes for $\gamma\gamma jj$ Production

The production of $\gamma\gamma jj$ from proton-proton collisions is in total a $2 \rightarrow 4$ process. This Process contains either diagrmans with four EW vertices or two EW and two QCD vertices. Only the purely EW diagrams contain any vector boson (VB) self interaction, and therefore can contain the quartic $WW\gamma\gamma$ this thesis focuses on. In the QCD diagrams only the photons are produced via EW vertices. To produce MC simulations, that are comparable to actual ATLAS data, it is necessary to consider the QCD $\gamma\gamma jj$, as no-reducible background, as well. Below the possible leading order (LO) processes for EW $\gamma\gamma jj$ production from two partons and some exemplary diagrams for the mixed processes can be found. The only diagrams containing any VB self-interaction are seen in fig.2.3, where only the right diagram contains the vertex this thesis focuses on. The exact processes which, in fig.2.3b, are only referred to as (?), are

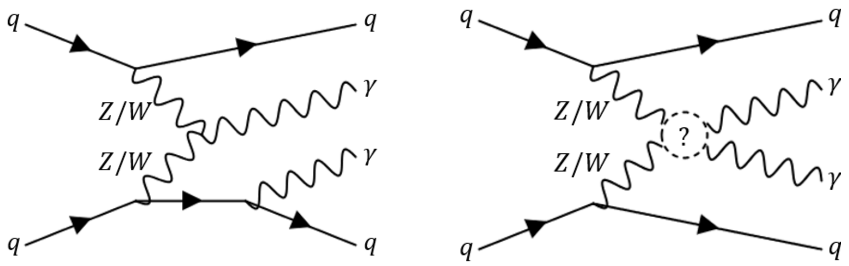

(a) Vector Boson Fusion

(b) Vector Boson Scattering

Figure 2.3: Diagrams that include VB self-interaction

displayed in fig.2.6. Other processes containing only EW vertices are shown in fig.2.4. The processes shown in (fiq.2.5) are examples of the possible processes which contain both QCD and EW vertices

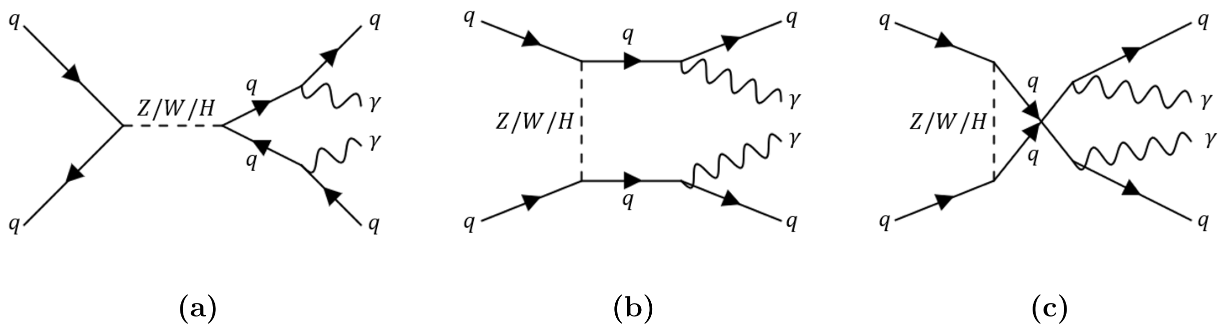

Figure 2.4: Diagrams with only EW vertices but not Vector Boson self-interaction

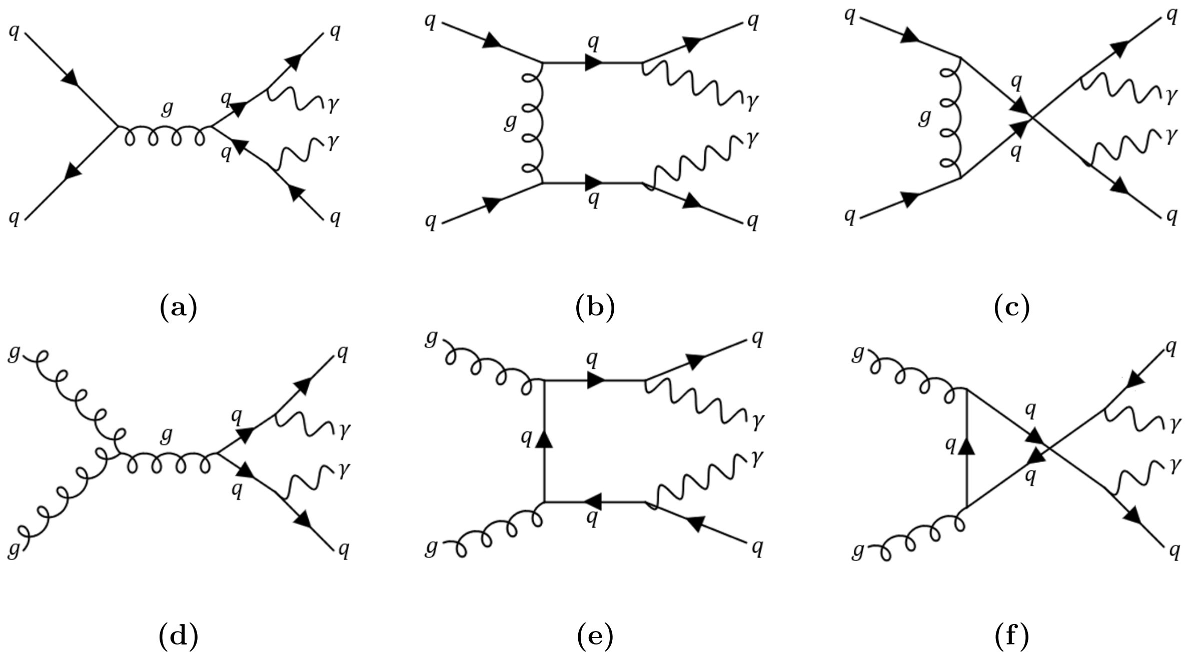

Figure 2.5: Diagrams with both QCD and EW vertices

While a trilinear vertex, in the EW interaction is proportional to $\sim e$, a quartic vertex is proportinal to $\sim e^2$, as shown in the EW Lagrangian [20]. Because of this a quartic EW vertex can occure in multiple ways. Depending on the interacting VB, the interaction can happen directly, or via an additional, virtual VB or Higgs boson, as seen below in fig.2.6 In the case of the SM $WW\gamma\gamma$ vertex, the interaction can only happen, if all vertices include an electrically charged particle, since the photons can only interact with those. By extending the SM with an EFT, as explained in section 2.4, additional vertices without charged particles can appear.

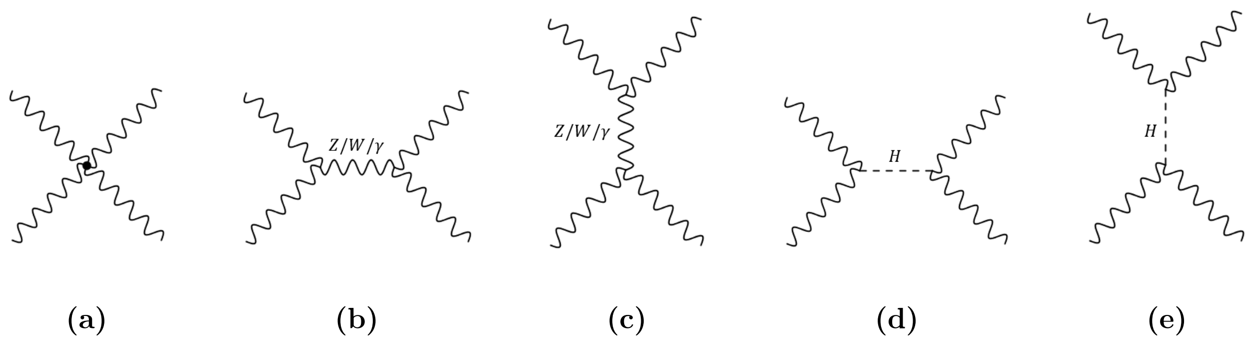

Figure 2.6: Possibilities for the $WW\gamma\gamma$ Interaction

2.4 Extending the Standard Model

The current Standard Model (SM) has been proven not to be the fundamental theory of everything. It is not able to explain gravity, dark matter and even deviations from its predictions of some properties seem to exist, see g-2 experiment [21]. To be able to predict effects of these Beyond Standard Model (BSM) physics, without having the knowledge of the precise underlying theory, Effective Field Theories (EFTs) [22, 23] are used. These theories are formulated mostly model independent meaning with as few and generic assumptions as possible. EFTs fulfill the requirements of a relativistic quantum field theory (QFT), but describe nature only in a certain range of validity, defined by the used energy scale Λ. Therefore EFTs are just a parameterization of the effects of the true underlying theory, which is unknown.

2.4.1 Mathematical formulation of an EFT

To extend a known theory, so-called bottom-up EFT approaches are used. These work by parameterizing the extension by manually adding new operators of higher mass dimensions to the known Lagrangian. These operators represent vertices in Feynman-diagrams that often do not exist within the SM and could in reality be comprised of multiple vertices of an unknown interaction. The known theory still holds in the low energy regime, and the extension only really contributes in the high energy regime. The Lagrangian of the EFT expansion of the SM looks as follows:

$$\mathcal{L}_{EFT} \; = \; \mathcal{L}_{SM} + \sum_{n=5}^{\infty} \sum_{i=0}^{N_n} \frac{f_i^{(n)}}{\Lambda^{n-4}} \mathcal{O}_i^{(n)} \tag{2.25}$$

The equation contains the SM Lagrangian, higher dimensional operators $(O)_i^{(n)}$, the Wilson coefficients $f_i^{(n)}$, the energy scale Λ and N_n, the number of terms at a given dimension n. Therefore, the expansion introduces an infinite number of new parameters. For the expansion to actually be applicable, two conditions have to be fulfilled. First, the number of parameters to describe interactions at any dimension n, to obtain a experimentally testable result, has to be finite. Secondly the contribution of any term of order (n+1) cannot exceed the contribution of a term of order n. For low energies this will easily be the case, but as contributions of higher dimension operators rise as the experimentally accessible energy $\sqrt{s}$ approaches Λ, this series breaks down. It is also to be noted, that EFTs are manually designed to approximate nature. Because of this, the theory is not necessarily UV-complete, which results in violations of unitarity, which has to be manually accounted for. This is done by adding a formalism that prevents the scattering amplitudes from approaching infinity at high energies. One of these formalisms is called "Clipping Unitarisation" and introduces a new parameter, the clipping energy, below which unitarity is always preserved and above which the EFT contributions are set to zero. The details of this approach are not further discussed in this thesis. Bottom-up EFTs have already proven to be useful in the past, e.g. Fermi's theory for the β-decay [24] can be classified as one. Fermi modeled a quartic vertex of the fermions (fig.2.7a) that participate in this process, thus neglecting the W boson which is exchanged in this interaction (fig.2.7b). This is how he was able to quantify this process more than 30 years before the prediction of the W and Z bosons in the theory of electroweak interaction.

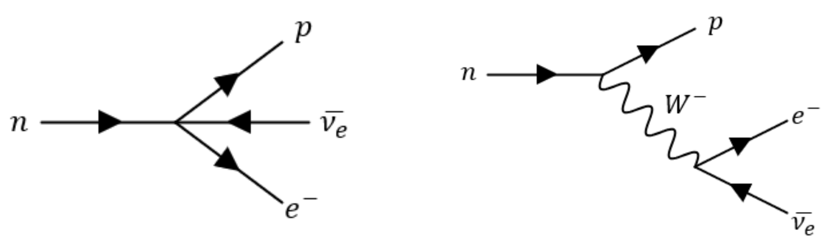

(a) β-decay via Fermi interaction

(b) β-decay via W-Boson

Figure 2.7: β-decay as described by (a) Fermi interaction, (b) weak interaction

2.4.2 Operators

The newly introduced EFT operators have to preserve the symmetries within the SM [22]. This means the operators, which consist of the gauge fields and their covariant derivatives, have to satisfy the $SU(3)_C \otimes SU(2)_L \otimes U(1)_Y$ gauge symmetry and Lorentz invariance and all conservation laws connected to these. The lowest dimension operator to fulfill the requirement is one dim-5 operator, which can be interpreted as the Majorana Mass term for neutrinos [25]. The next higher dimensional operators to preserve the symmetries are dim-6 operators. Those operators' contributions have been studied extensively in LEP and early LHC runs, and have been found to mainly influence triple self couplings and only affect quartic self couplings to a lesser extend. Operators of dimension 7 have been found to all violate baryon number conservation, which is why only dim-8 operators can be used again [26]. These should contribute mostly to quartic vertices and will therefore be the operators considered in this thesis. The Lagrangian from (eq.2.25) with only dim-8 operators added looks like this:

$$\mathcal{L} = \mathcal{L}_{SM} + \sum_i \frac{f_i^{(8)}}{\Lambda^4} \mathcal{O}_i^{(8)} \tag{2.26}$$

The dim-8 operators [27, 28] can be categorised in 3 classes: S,M and T. The S Operators contain only the covariant derivatives of the Higgs field ($D_\mu \Phi$) and affect vertices with only longitudinally polarized bosons, and therefore no photons, so they are not relevant for this study. The M operators consist of the field strength tensors $\hat{W}_{\mu\nu} = \sum_a W^a_{\mu\nu} \frac{\sigma^a}{2}$ and contribute to vertices of mixed polarizations, which is the case for the $WW\gamma\gamma$ vertex. The last group contains only field strength tensors, and affect only transversely polarized vertices, so the operators which contain both the $\hat{W}^{\mu\nu}$ fields and the $B^{\mu\nu}$ field contribute. The operators that contribute to the $WW\gamma\gamma$ vertex are [29]:

$$\begin{aligned}
\mathcal{O}_{M,0} &= Tr[\hat{W}_{\mu\nu}\hat{W}^{\mu\nu}] \cdot [(D_\beta\Phi)^\dagger D^\beta\Phi] & \mathcal{O}_{M,1} &= Tr[\hat{W}_{\mu\nu}\hat{W}^{\nu\beta}] \cdot [(D_\beta\Phi)^\dagger D^\mu\Phi] \\
\mathcal{O}_{M,2} &= [B_{\mu\nu}B^{\mu\nu}] \cdot [(D_\beta\Phi)^\dagger D^\beta\Phi] & \mathcal{O}_{M,3} &= [B_{\mu\nu}B^{\nu\beta}] \cdot [(D_\beta\Phi)^\dagger D^\mu\Phi] \\
\mathcal{O}_{M,4} &= [(D_\mu\Phi)^\dagger \hat{W}_{\beta\nu} D^\mu\Phi] \cdot B^{\beta\nu} & \mathcal{O}_{M,5} &= [(D_\mu\Phi)^\dagger \hat{W}_{\beta\nu} D^\nu\Phi] \cdot B^{\beta\mu} + h.c. \\
\mathcal{O}_{M,7} &= [(D_\mu\Phi)^\dagger \hat{W}_{\beta\nu} \hat{W}^{\beta\mu} D^\nu\Phi] & &
\end{aligned}$$

$$\begin{aligned}
\mathcal{O}_{T,0} &= Tr[\hat{W}_{\mu\nu}\hat{W}^{\mu\nu}] \cdot Tr[\hat{W}_{\alpha\beta}\hat{W}^{\alpha\beta}] & \mathcal{O}_{T,1} &= Tr[\hat{W}_{\alpha\nu}\hat{W}^{\mu\beta}] \cdot Tr[\hat{W}_{\mu\beta}\hat{W}^{\alpha\nu}] \\
\mathcal{O}_{T,2} &= Tr[\hat{W}_{\alpha\mu}\hat{W}^{\mu\beta}] \cdot Tr[\hat{W}_{\beta\nu}\hat{W}^{\nu\alpha}] & \mathcal{O}_{T,5} &= Tr[\hat{W}_{\mu\nu}\hat{W}^{\mu\nu}] \cdot B_{\alpha\beta}B^{\alpha\beta} \\
\mathcal{O}_{T,6} &= Tr[\hat{W}_{\alpha\nu}\hat{W}^{\mu\beta}] \cdot B_{\mu\beta}B^{\alpha\nu} & \mathcal{O}_{T,7} &= Tr[\hat{W}_{\alpha\mu}\hat{W}^{\mu\beta}] \cdot B_{\beta\nu}B^{\nu\alpha}
\end{aligned}$$

In some papers an additional operator $\mathcal{O}_{M,6}$ is listed, which was found to be redundant [28].

2.4.3 Wilson Coefficients

The Wilson coefficients f_i, as seen in eq.2.26, can be interpreted as something similar to a coupling strength of the dim-8 operator. The Wilson coefficients can only be constrained in combination with the energy scale as $c_i = \frac{f_i}{\Lambda^{-4}}$. Below is a table of current limits of the current limits for the relevant Wilson coefficients as determined at ATLAS for $\sqrt{s} = 13\,\text{TeV}$. Since this thesis is not focused on improving these limits, but rather to see if improvements would be possible with the studied process, only the average of the limits is used in this thesis.

The values in the above table where measured in $W\gamma jj$ production. In the original paper [2] the limits where measured for various different variables, but here only the strictest limits are used.

Coefficient	Observed 95% CL Limit [TeV^{-4}]	Average [TeV^{-4}]
f_{M0}/Λ^{-4}	[23.99,23.75]	23.87
f_{M1}/Λ^{-4}	[36.91,37.89]	37.4
f_{M2}/Λ^{-4}	[8.63,8.59]	8.61
f_{M3}/Λ^{-4}	[13.42,13.67]	13.545
f_{M4}/Λ^{-4}	[15.45,15.46]	15.455
f_{M5}/Λ^{-4}	[13.95,12.26]	13.105
f_{M7}/Λ^{-4}	[66.21,65.26]	65.735
f_{T0}/Λ^{-4}	[1.75,1.8]	1.775
f_{T1}/Λ^{-4}	[1.09,1.16]	1.125
f_{T2}/Λ^{-4}	[3.14,3.46]	3.3
f_{T5}/Λ^{-4}	[1.24,1.25]	1.245
f_{T6}/Λ^{-4}	[1.04,1.06]	1.05
f_{T7}/Λ^{-4}	[2.74,2.82]	2.78

Table 2.1: Wilson Coefficients for $WW\gamma\gamma$ coupling, measured via p_T^l distribution for the M-Operators and p_T^{jj} distribution for the T-Operators [2]

2.4.4 Decomposition

The differential cross-section of a process is proportional to the square of the absolute value of the matrix element (ME):

$$\frac{d\sigma}{d\Omega} \sim |M|^2 \tag{2.27}$$

In the case of a SM EFT, the ME is comprised of the SM ME and an additional EFT ME: $M = M_{SM} + M_{EFT}$. With this the differential cross section can be decomposed into multiple contributions:

$$\frac{d\sigma}{d\Omega} \sim |M|^2 = |M_{SM} + M_{EFT}|^2 \tag{2.28}$$

$$= |M_{SM}|^2 + M_{SM}M_{EFT} + |M_{EFT}|^2 \tag{2.29}$$

The first term is the SM contribution, the second term is the linear EFT contribution, or interference term and is proportional to Λ^{-4}. Contrary to the other terms, this one can be negative, thus leading to a smaller differential cross-section. The last term is the quadratic EFT contribution, which is proportional to Λ^{-8} and thus is the same order of magnitude as the contribution of the linear part of dim-12 Operators. This can lead to uncertainties for the cross-section measurements due to interferences from the dim-12 contribution not taken into account. For this reason the analysis is done for SM + interference and full dim8-EFT contribution. For the event generation these contributions are selected by using the "interaction order" syntax, which is further explained in section 3.2.

3 Methods

3.1 Event Generation

To study the effects of the EFT in proton-proton collisions, the MC event generator SHERPA [30, 1] version 3.0.0beta1 is used. This event generator is able to simulate high energy interactions in multiple types of collisions, especially hadron-hadron collisions. This is done by simulating the processes in MC steps, where each step represents one phase of the process. The first step is the hard process [1], which can be directly calculated from the matrix element generated by the ME generator Comix [31]. Here this is the production of two jets and photons from two incoming partons. To obtain more physical results, SHERPA then simulates additional steps such as parton showering, hadronization, multi parton interactions and some others. SHERPA can take multiple different inputs into account, such as the beam energy, or different parton distribution functions. In this thesis, the processes are simulated with the ME generator Comix and the phase space generator Phasic, which calculate and integrate tree level amplitudes. To include the dim-8 EFT, an additional model has to be included in SHERPA, to extend the implemented SM calculations by the additional dim-8 operators. This additional Model is called SM_Ltotal_Ind5v2020v2_UFO [29]. Originally it was planned, that for the SM processes, 10 million prior generated events would be used, which have been used in other analyses and are most likely correct. Unfortunately towards the end of this thesis, it was found, that the EFT model generates events which are not compatible with the events generated with standard SHERPA. Therefore for the SM analysis only 2 million events were used, to meet the time-frame of this thesis. The events produced with the EFT model were generated with runcards similar to the examples found in A. For each EFT operator 2 million events were generated for the full EFT contribution and for the SM + linear contribution respectively.

3.2 Runcards

To generate events, SHERPA needs inputs that specify the process some details about the way this process is supposed to be simulated. These inputs are provided as so called runcards, which are files in the .yaml format. In these runcards numerous settings can be made, for example the beam energy, if the events will be weighted, or which renomalizations scales are to be used. All the setting mentioned below are explained in more detail in the SHERPA

manual [32]
To imitate LHC run 2, the beam settings are "BEAMS: 2212" and "BEAM_ENERGIES: 6500", where the first setting defines the proton beams and the second setting gives a center of mass energy of $\sqrt{s} = 13\,\text{TeV}$. The integration is done with a minimum of 25000 iterations and an error of 5 %. For the EW diagrams, the reconstruction of the jets assumes only QCD interactions, which is achieved by the "EXCLUSIVE_CLUSTER_MODE=1" setting. Also the jets are not supposed to exchange any color charge in this process, which is secured by the setting "CSS_CSMODE: 1". Multiple settings are made to increase the integration and event generation performance: "CDXS_VSOPT:5", "MEPS: CORE_SCALE: VAR{Abs2(p[2]+p[3])} and "SCALES: METS{MU_F2}{MU_R2}{MU_Q2}", where the two latter settings affect the renormalization scales of the process and core process and stop clustering if no corresponding combination for parton shower branching can be found. As mentioned previously the SM events generated with the EFT model do not fit with the events generated with standard SHERPA. One difference that was discussed to maybe be the cause of the deviations between the generation of SM events with and without the EFT model is the change of "VBF" to "METS" is the "SCALES" setting. Unfortunately this was found to not be the cause of the deviations as can be seen in fig.3.1. Here the cross section distribution of the pseudorapidity of the first leading photon can be seen. While the graphs for the events produced without the model (red, blue) are very close to each other, the events produced with the EFT model deviate heavily, changing the shape of the plot. Therefore the "SCALES" setting seems to not be the reason for the problems.

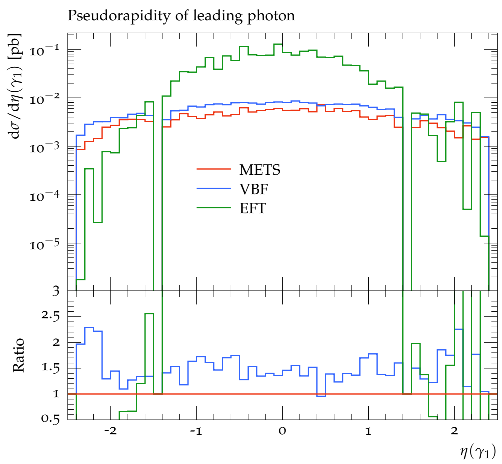

Figure 3.1: Plot of the differential cross section against the pseudorapidity of the first leading photon. Red and blue graphs produced without the EFT model, but different Settings for the renormalization scale (VBF, METS). Green graph produced with the EFT model and METS setting

To increase the number of events that pass the analysis cuts (see section 3.3), some preselections are made in the generation process, which are less strict than the analysis cuts. Those selectors are implemented for the photons and jets created in the process. The photons have to have a minimum transverse momentum of $p_{T_{\gamma 1}} > 20\,\mathrm{GeV}$ and $p_{T_{\gamma 2}} > 18\,\mathrm{GeV}$. For the jet selection, the FastJet plugin [33] with the Anti-k_t algorithm [34] was used. This selected events with at least 2 jets, with a transverse momentum of $p_{T_j} > 20\,\mathrm{GeV}$ and a radial parameter of $\Delta R > 0.4$.

While configuring the runcards it was found that the standard phase space integrator used by Comix, is not able to compute the quadratic contribution of the EFT operators. This seems to be due to some recent changes that introduced a bug, which could not be fixed in the time frame of this thesis. Because of this, another phase space integrator, called RAMBO [35], was used to generate the events with EFT contribution. Since this integrator is not optimized as well as the standard integrator, problems could arise in the form of calculating a non diverging cross section, leading to nonsensical results. Luckily the deviations of the cross sections of the generated events where found to be in the ranges of a few percent, which is precise enough for the means of this thesis. The quarks involved in the processes were assumed to be massless, since the ME generator could not find a process for massive quarks. This assumption should not change the results drastically, since the jets momenta will be much larger than the masses, therefore the masses can be neglected.

As mentioned in section 2.4.4 the simulation is done once with the full EFT contribution and once with only the interference term. To achieve this, the maximum process order has to be defined. The process order specifies the proportionality of the matrix element to the coupling constants α_i. In the SM this also represents the number of contributing vertices of the interaction, where a quartic EW vertex has the proportionality of two vertices, as mentioned in section 2.3. For an EFT vertex the Wilson coefficient can be thought of as the coupling constant. Since all the dim-8 operators represent quartic vertices and the Wilson coefficient is not given as squared value, these vertices are proportional to $f_{EFT} \sim \alpha_{EFT}$. For the $WW\gamma\gamma$ vertex this would look as follows:

$$
\begin{array}{ccccccc}
|M_{SM} + M_{EFT}|^2 & = & |M_{SM}|^2 & + & M_{SM}M_{EFT} & + & |M_{EFT}|^2 \\
 & & \sim \alpha_{EW}^2 & & \sim \alpha_{EW}^1 \alpha_{EFT}^{1/2} & & \sim \alpha_{EFT}^1
\end{array}
$$

So to generate a quartic EW vertex including the SM and the linear EFT contribution, diagrams of the order $\alpha_{EW}^2 \alpha_{EFT}^0$ and $\alpha_{EW}^1 \alpha_{EFT}^{1/2}$ would have to be considered. To include the quadratic EFT contribution also a vertex of order $\alpha_{EW}^0 \alpha_{EFT}^1$ would need to be allowed. This is achieved with the "Max_Order" setting. To generate the full $\gamma\gamma jj$ production processes, the remaining vertices have to be included as well. The SM EW production has the proportionality $\sim \alpha_{EW}^4 \alpha_{EFT}^0$, the linear process $\sim \alpha_{EW}^3 \alpha_{EFT}^{1/2}$ and the quadratic contribution $\sim \alpha_{EW}^2 \alpha_{EFT}^1$.

To have truly compatible data it would have also been necessary to generate the QCD events with the EFT model to avoid any deviations created by this model. Unfortunately the integration time of the QCD processes was too high, so it was not finished until the end of the time of this thesis. This is due to the QCD process containing not just the 2->4 $\gamma\gamma jj$ production, but also processes with additional jets. It also is questionable of the events produced within the model would have been useful since for these processes, diagrams of NLO or containing loops would have a significant contribution, yet the EFT model did not allow for the generation of events with those additional diagrams. Because of this, for the calculation of the uncertainties the QCD events generated without the EFT model were used, though it is likely that the cross section of those is too low.

3.3 Data Analysis

The Analysis of the particle event data generated by SHERPA is done with the Rivet analysis toolkit [36, 37], which is specifically designed for the analysis of particle physics MC data. Since the collisions of particles are quantum mechanical processes, it is not possible to identify the chain of interactions which lead to the measured events, but only to make statistical statements about the likelihood of a certain processes' contribution. In $VVjj$ production, VBS processes have a distinct signature, with high invariant masses (m_{jj}) and large rapidity differences (ΔY_{jj}) of the jets [38]. But each VBS process has additional signatures in various observables, that allow for a better distinction between them. So to maximise the number of events, that are correctly counted as signal events, certain cuts in the processes phase space are applied. These cuts are applied on the rapidities, pseudorapidities and angular distance as defined in section 2.1.2, as well as transverse momenta (p_T) and invariant mass of the jets. Additionally on the number of jets in the gap between the leading jets N_{jets}^{gap} cuts are applied, as well as on the centrality defined in eq.3.1.

$$\xi = \frac{|Y_{\gamma\gamma} - (Y_{j1} + Y_{j2})/2|}{\Delta Y_{jj}} \quad \text{with:} \quad \Delta Y_{jj} = |Y_{j1} - Y_{j2}| \tag{3.1}$$

$Y_{\gamma\gamma}$ being the rapidity of the added four momenta of both photons.
The number of gap jets is determined by identifying additional jets, besides the leading jets. The leading jets' rapidities are used as upper and lower bounds for the jets. The additional jet is counted as a gap jet if:

$$lower + 0.1 < Y_{j3} < upper - 0.1. \tag{3.2}$$

The invariant mass of two particles is calculated as:

$$m_{12} = \sqrt{(E_1 + E_2)^2 - (\vec{p}_1 + \vec{p}_2)^2}. \tag{3.3}$$

The leading jets and photons are labeled 1 and 2, based on their transverse momentum, where the particle with the higher p_T is labeled particle 1. The exact cuts applied can be found in table 3.1. The Analysis code and cuts were taken from an ongoing ATLAS SM VBS $\gamma\gamma jj$

Analysis, so no citation is possible.

Observable	event included if
p_{T,γ_1}	$\geq 40\,\mathrm{GeV}$
p_{T,γ_2}	$\geq 30\,\mathrm{GeV}$
$\lvert\eta_{\gamma_{1,2}}\rvert$	≤ 2.37
	exluding: $1.37 < \lvert\eta_{\gamma_{1,2}}\rvert < 1.52$
$p_{T,j_{1,2}}$	$\geq 30\,\mathrm{GeV}$
$\lvert Y_{j_{1,2}}\rvert$	≤ 4.4
$\Delta R_{\gamma\gamma}$	≥ 0.4
$\Delta R_{\gamma j}$	≥ 0.6
m_{jj}	$\geq 500\,\mathrm{GeV}$
$Y_{j_1} * Y_{j_2}$	< 0
ΔY_{jj}	≥ 2.0
N_{jets}^{gap}	$= 0$
ξ	≤ 0.5

Table 3.1: Cuts applied to the analysis

The goal of this thesis is to visually compare the differential cross sections of processes with EFT contribution to SM processes. This is done to see if improvements on the limits of the Wilson coefficients could be expected with processes including the $WW\gamma\gamma$ vertex, or if technical limitations do not allow for that. For this the differential cross sections of the EFT processes are plotted with the SM processes. If the EFT cross sections lie outside the error margins of SM processes, improvements on the limits could be possible. To make this comparison meaningful, it is necessary to determine the uncertainties of the SM process. For this thesis, the uncertainties considered are the statistical uncertainties of the VBS signal (S) and QCD background (B) and an additional systematic uncertainty for the background, which comes from estimations of errors for renormalization scale variations. The produced events are assumed to be Poisson distributed. Therefore the statistical uncertainty for each bin can be calculated by using the number of events per bin. With eq.2.1, the expected Number of events (N_{bin}) per bin can be calculated where the total cross section is the differential cross section the bin represents, and the integrated luminosity is $139\,\mathrm{fb}^{-1}$, as given for LHC run 2.

$$N_{bin} = \sigma_{bin} \cdot L_{LHC} = \int_{x_1}^{x_2} \frac{d\sigma}{dx} dx \cdot L_{LHC} \qquad \text{with } x_{1,2} \text{ being the bin edges.} \tag{3.4}$$

With this the variance of each bin, and therefore the standard deviation can be calculated as

$$(\Delta N_{bin})^2 = N_{bin} \;\Rightarrow\; \Delta N_{bin} = \sqrt{N_{bin}} \tag{3.5}$$

Since in this thesis simulated data is used, the statistical uncertainties for the entire data (D) and for the QCD background are considered. Therefore the statistical uncertainties are:

$$\Delta N_{D,stat} = \sqrt{N_D} = \sqrt{N_S + N_B} \quad \text{and} \quad \Delta N_{B,stat} = \sqrt{N_B} \tag{3.6}$$

As systematic uncertainties only ones that stem from renormalization scale variations in the QCD background are considered, to fit the scope of this thesis. For di-photon production from two protons the corrections for LO hard processes, as considered in this thesis, are assumed to be in the range of $\sim 30\%$ [39]. With this, the systematic uncertainty can be calculated as 30% of the background events:

$$\Delta N_{B,syst} = 0.3 \cdot N_{QCD}. \tag{3.7}$$

To calculate the absolute uncertainty for the differential cross section in each bin, the relative uncertainties of the events are used:

$$\Delta \sigma_{bin} = \sigma_{S,bin} \cdot \frac{\Delta N_{bin}}{N_{S,bin}} \tag{3.8}$$

Thus, the total uncertainty for the Signal can be calculated as:

$$\begin{aligned} \Delta \sigma_S &= \sigma_S \sqrt{\left(\frac{\Delta N_{D,stat}}{N_S}\right)^2 + \left(\frac{\Delta N_{B,stat}}{N_S}\right)^2 + \left(\frac{\Delta N_{B,syst}}{N_S}\right)^2} && (3.9) \\ &= \sigma_S \sqrt{\left(\frac{\sqrt{N_S + N_B}}{N_S}\right)^2 + \left(\frac{\sqrt{N_B}}{N_S}\right)^2 + \left(\frac{0.3 \cdot N_B}{N_S}\right)^2} && (3.10) \\ &= \frac{\sigma_S}{N_S} \sqrt{N_S + 2N_B + (0.3 \cdot N_B)^2}. && (3.11) \end{aligned}$$

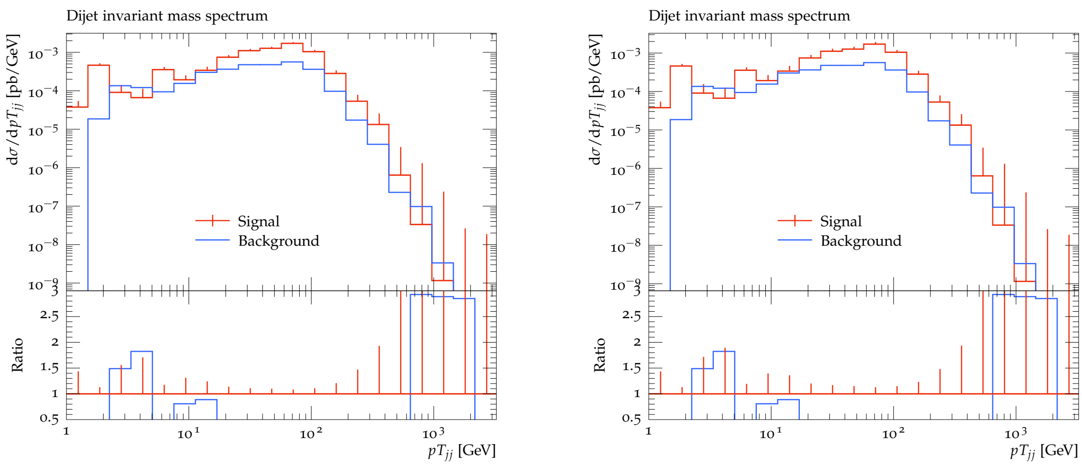

(a) without systematic uncertainties

(b) with systematic uncertainties

Figure 3.2: $p_{T_{jj}}$ plots for the VBS Signal and the QCD backround with statistical and once with and once without systematic uncertainties

In fig.3.2 the uncertainties for $p_{T_{jj}}$ can be seen. It is noticeable that the uncertainties at high differential cross sections are barely visible and only get significantly high at low cross sections. It can also bee seen that the uncertainties are dominated by the statistical uncertainties, and that the systematic uncertainty does not contribute much to the overall uncertainty, as it is almost identical in both plots. Since it would have been expected, that the QCD background has a cross section higher than the EW signal, it also would have been expected, that the uncertainties would be larger due to the increase in both statistical and systematic uncertainties. Additionally, it can be seen in eq.3.11 that $\Delta\sigma_S \sim N_B$. This means that if the QCD background was compatible to the signal data, the total uncertainty would be dominated by the systematic uncertainty instead of the statistical uncertainty. This leads to the conclusion, that the uncertainties are underestimated here. Unfortunately to fix this it would at least be necessary to generate the QCD events using the EFT model. As mentioned before, this was not possible in the time-frame of this thesis, as the integration time for this is very high. Therefore in this thesis the uncertainties will be used as they are shown here.

4 Results

In this section the results of the simulations are shown in the form of bin plots of the processes with EFT contribution and the SM processes. The plots show three lines, where the red line represents the SM, the blue line represents the processes with full EFT contribution, and green represents only the linear EFT contribution. Additionally the uncertainty margins of the SM signal are plotted to see if the EFT processes lie within or outside of those. All plots show the differential cross section $\frac{d\sigma}{dx}$ where x represents the observable plotted on the x-axis, e.g. the added transverse momentum of the jets $p_{T_{jj}}$. The bins contain the differential cross section integrated over the bin width. The plots shown here are only a selection of all plots made for only some of the operators. This is to keep the amount of plots reasonable and because for most of the operators the plots look similar. The plots not chosen for this results section can be found in (section A). As mentioned before, during the final stages of this thesis, a problem with the events from the EFT model was found, which resulted in the cross sections of the SM events generated without the EFT model and the EFT events not being compatible. Because of this only data from events generated with the EFT model is considered here. The deviations of the EFT model events and the standard SHERPA events can be seen in fig.4.1 where the cross section of the SM EW predictions from both methods are plotted. It is visible that not only do the cross sections differ strongly as seen in fig.4.1a, but also the shape of the plots can be heavily affected, as shown in fig.4.1b. The comparison of the cross sections of the SM and the EFT predictions is made under the assumption that the overall effects would be similar if the data were correct. Unfortunately the mismatch could not be further investigated due to the time constraint of this project. The comparison between EFT and SM predictions should be repeated once consistent data becomes available in order to ensure the accuracy of the results

First it can be noted that the applied analysis cuts were effective and can be seen in the plots of the respective quantities in fig.4.2. For fig.4.2a and fig.4.2b the cuts are easily visible. For fig.4.2d the cut is not as clear, since the bin widths are not set in a way that results in a bin edge at 500 GeV, but slightly behind that value. This leads to the bin before 500 GeV having a non-zero differential cross section. However it is also visible that there is a steep increase from this bin to the next, so most events were cut out and the cut was effective. In fig.4.2c the cuts can be seen once in the first and last bin being empty and also the bins in the exclusion ranges being empty. Also the cuts in the transverse momentum of the jets lead

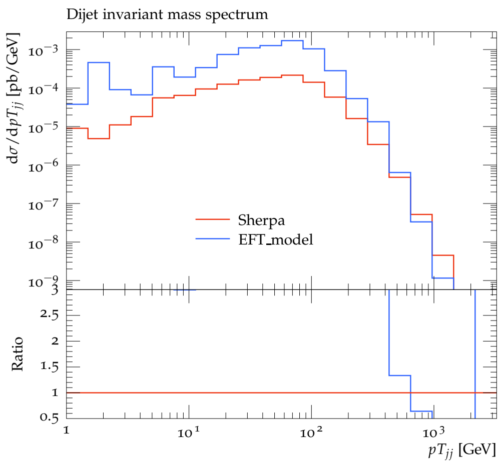

(a) $p_{T_{jj}}$ plot of the SM EW cross sections by the standard SHERPA event generation and the EFT model

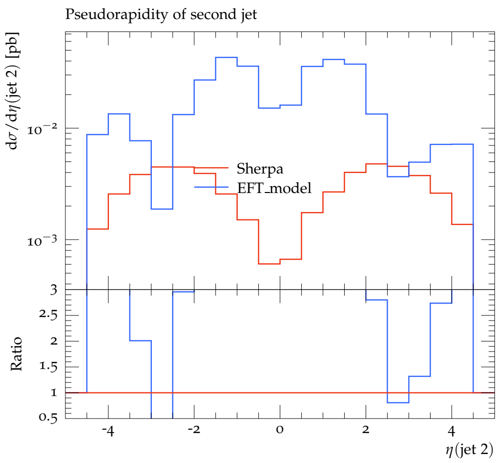

(b) η_{j_2} plot of the SM EW cross sections by the standard SHERPA event generation and the EFT model

Figure 4.1: Comparison of cross sections from events generated with standard SHERPA and the EFT model

to the jets being in ultra-relativistic energy ranges ($E_j \gg m_j \;\Rightarrow E_j \approx p_j$), which leads to the rapidity and pseudorapidity being almost equal as mentioned in section 2.1.2. This can also be seen in fig.4.3. In fig.4.3a and fig.4.3b the plots for the differential cross section against the rapidity and pseudorapidity of the first leading jets are shown, which look very similar with only minor deviations. The same can be seen in fig.4.3c and fig.4.3d. Here the shapes of the plots are near identical for $|\Delta Y_{jj}|$ and $|\Delta\eta_{jj}|$, and the differential cross sections in the rapidity plot is about twice as high as in the plot for the pseudorapidity for either $\Delta\eta_{jj} \gtrless 0$. This leads to the conclusion that the assumption made in the event generation that the particles are massless is a good approximation and does not cause any major deviations. In fig.4.4 the different contributions of the M and T EFT operators are plotted for $m_{\gamma\gamma}$. It can be seen that the EFT contributions only change the differential cross section in the high energy region. The deviations in the low $m_{\gamma\gamma}$ region are due to the MC generation and would disappear with a higher number of events. In the high energy region, the differential cross section is changed for the full contributions for some of the M operators. Furthermore for the linear contributions of some of the T operators and the full contributions of all T operators an increase of the differential cross section can be seen here. The increase is the highest for the full contributions of the T operators, where the shape of the plot is visibly changed in the high energy region. The total cross section of the SM prediction as obtained from the EFT model generation with applied analysis cuts is about 0.167 pb. This is too high, since for this process with the applied cuts, the total cross section was determined as 25 fb in simulations without the EFT model. That means the total cross section used here is about 6.7 times higher than expected. This shows once more, that there seems to be some error within the generation of the events or the used EFT model. In table 4.1 the total cross sections of the EFT operators with linear and full contribution can be seen. This shows that the EFT operators do not increase the total cross section very much. In cases, where the total cross section is decreased, the MC generation of the events is likely the cause, which means that this effect would disappear with a higher number of events.

As mentioned above, the effects introduced by the EFT operators are not very large. Since the existing limits for the Wilson coefficients are already very narrow, this was to be expected, as huge deviations especially at high differential cross sections could probably not be corrected within the EFT limits. In fig.4.5 some plots for the M1 operator can be seen. In the plots for the invariant masses of jets and photons the deviations are mostly very small and lie within the SM uncertainties. For high invariant jet masses there are some larger deviations which mostly still lie within the SM uncertainties. For the one bin at about $1700\,\mathrm{GeV} < m_{jj} < 2200\,\mathrm{GeV}$ with larger deviation, this deviation also has a large uncertainty due to the MC generation of the events. For the combined transverse momenta of the jets and photons there are some deviations in the low energy region $< 20\,\mathrm{GeV}$. These are also likely due to the MC generation, which is visible by the strong fluctuations between the bins and would disappear with higher event numbers. In fig.4.6 plots for the M2 operator are shown. For the combined transverse momenta and the invariant mass of the jets the behaviour is very similar as for M1. However for the transverse momenta of the jets there seem to be some more interesting effects. Here the full EFT contributions seem to deviate more significantly from the SM prediction in the high energy ranges. This also cannot be entirely explained by the uncertainties due to the MC generation. In this region there seems to be another peak of the differential cross section after which it decreases again. This means this effect is not created by a unitarity violation which would happen at energies closer to the energy scale and would need to be fixed by applying a clipping energy, but rather is an effect the EFT operators predict. This effect is visible for all operators which contain the gauge field connected to the $U(Y)_1$ symmetry group $B^{\mu\nu}$, so M2, M3, M4, M5. It is strongest for those containing multiple instances of this field. However, this deviation is also located in a region with an already low differential cross section and therefore large statistical uncertainties. This leads to the deviations visible being within the uncertainty margins for the SM predictions, which means that the effect do not necessarily allow for improvements of the limits of the Wilson coefficients. Nevertheless, it is interesting to see these deviations as it shows that the $WW\gamma\gamma$ vertex truly is sensitive to these operators and would possibly allow for improvements in the future with higher energies and luminosities. For the T0 operator some plots are shown in fig.4.7. In the low energy region the behaviour of the differential cross section again does not differ much from the SM predictions. The plot for the invariant mass of the jets generally does not deviate too much from the SM prediction. The $p_{T_{jj}}$ and $p_{T_{\gamma\gamma}}$ plots already show some deviations of the full EFT contribution from the SM in the high energy region. Those, however mostly lie within, or barely outside of the SM uncertainties. For $m_{\gamma\gamma}$ and $p_{T_{\gamma 1/2}}$ this is not the case. The deviations of the full EFT contribution seen in those diagrams at high energies are clearly outside of the SM uncertainties. Especially for the transverse momenta of the single photons the EFT operator seems to noticeably affect the differential cross section, bringing it outside the uncertainty margins of the SM prediction. Again the EFT operator introduces additional peaks of the differential cross section which for T0 are located at about $p_{T_{\gamma 1}} = 1050\,\mathrm{GeV}$ and $p_{T_{\gamma 2}} = 900\,\mathrm{GeV}$. These deviations could allow for improvement of the EFT limits, though it would need to be confirm that the effects in the data produced by the EFT model would be the same relatively for the correct data. Additionally, a more sophisticated analysis would be needed to get the complete uncertainties for the SM prediction. For the T5 operator the plots can be found in fig.4.8. Here similar effects as for T0 can be seen. While for the jets the cross sections are barely affected, the plots for the photons clearly show the contribution of the EFT operator. The most significant effect again can be seen in the plots for the transverse momenta of the single photons. The effect here is even larger than for the T0 operator. For the T operators an equal observation can be made for the relation between the effects introduced by the EFT operator and the gauge fields the operator contains. As for the M operators, those which contain the $B^{\mu\nu}$ field produce larger effects than those that only contain the $W^{\mu\nu}_{1,2,3}$ fields. However, in contrast to the M operators where those that do not contain the $B^{\mu\nu}$ field do not produce any clearly visible contribution to the cross section, all T operators affect the cross section in a noticeable way. Overall it can be said that an improvement for the EFT limits could be possible by studying the process of di-photon production, more specifically those that contain the $WW\gamma\gamma$ vertex. But for this at least a more thoughtful analysis of the uncertainties would have to be done since in this thesis only the statistical uncertainties and the systematic uncertainty of the background signal were considered.

Operator	σ_{SM+Lin} [pb]	σ_{Full} [pb]
M0	0.162	0.147
M1	0.161	0.204
M2	0.168	0.164
M3	0.165	0.196
M4	0.177	0.154
M5	0.172	0.168
M7	0.160	0.175
T0	0.166	0.162
T1	0.172	0.180
T2	0.148	0.154
T5	0.189	0.188
T6	0.171	0.162
T7	0.208	0.181

Table 4.1: Total cross sections of the EW $\gamma\gamma jj$ production for the different EFT operators and contributions with applied phase space cuts

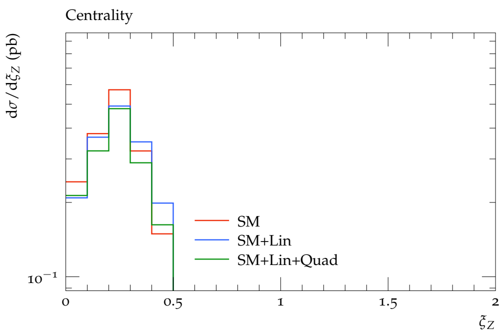

(a) Centrality cut for $\xi \geq 0.5$

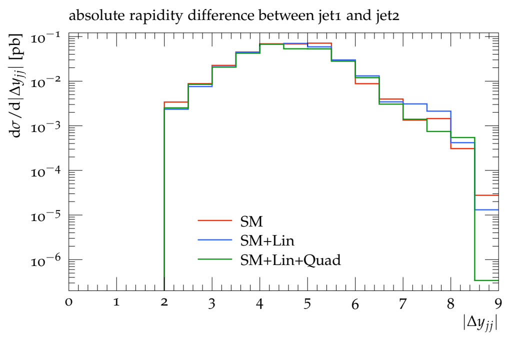

(b) Leading jet rapidity difference cut for $\Delta Y_{jj} \leq 2.0$

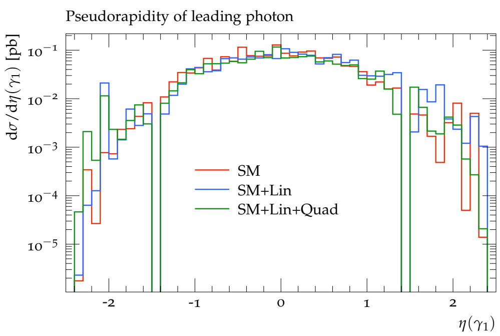

(c) First leading photon pseudorapidity cut for $|\eta_{\gamma_1}| \geq 2.37$ with exclusion of $1.37 < |\eta_{\gamma_1}| < 1.52$

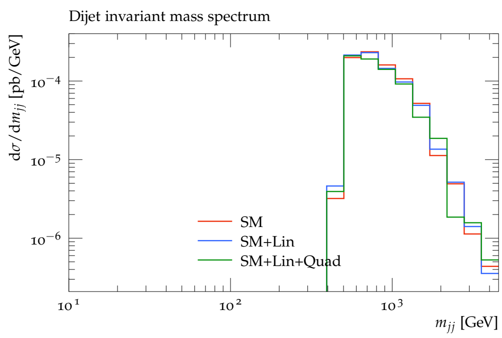

(d) Invariant leading jet mass cut for $m_{jj} \leq 500\,\text{GeV}$

Figure 4.2: Some plots for $\mathcal{L}_{M0}$ with visible analysis cuts

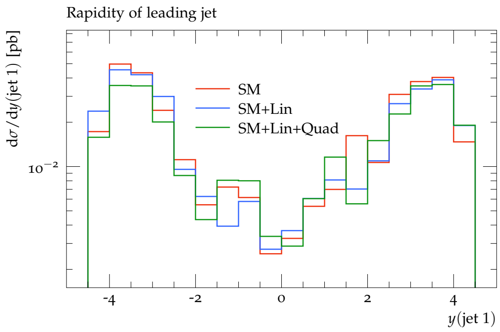

(a) Diff. cross section plotted against rapidity of first leading jet Y_{j_1}

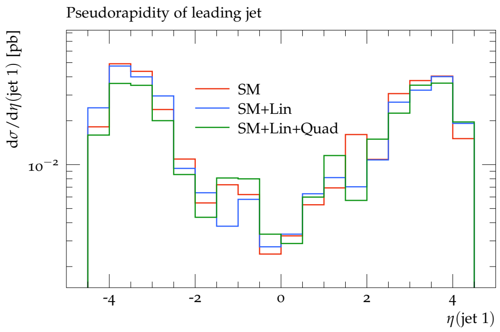

(b) Diff. cross section plotted against pseudorapidity of first leading jet η_{j_1}

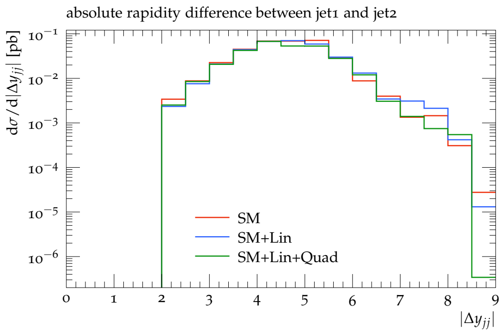

(c) Diff. cross section plotted against absolute rapidity difference of leading jets $|\Delta Y_{jj}|$

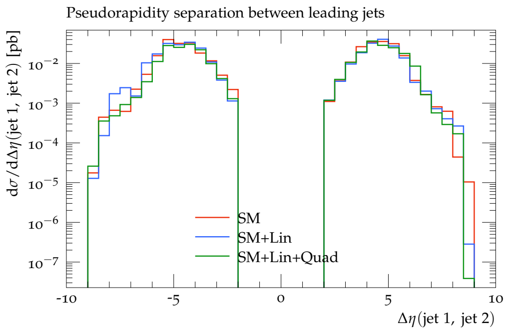

(d) Diff. cross section plotted against Pseudorapidity difference of leading jets

Figure 4.3: Plots for $\mathcal{L}_{M0}$ of Rapidity (left) and Pseudorapidity (right) of jets with visible similarities

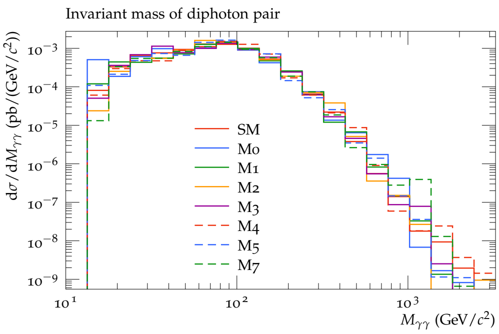

(a) Plot of $m_{\gamma\gamma}$ for linear EFT contribution of all M Operators plotted with the SM prediction

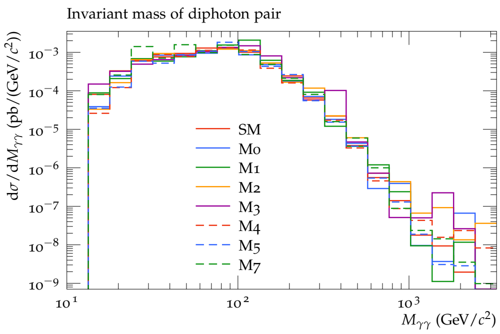

(b) Plot of $m_{\gamma\gamma}$ for full EFT contribution of all M Operators plotted with the SM prediction

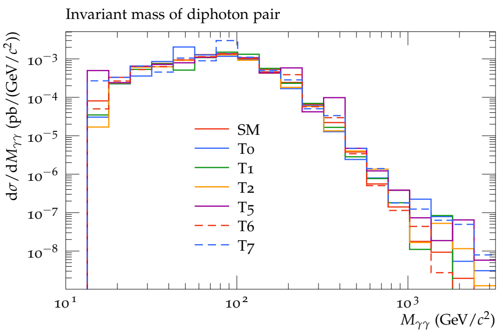

(c) Plot of $m_{\gamma\gamma}$ for linear EFT contribution of all T Operators plotted with the SM prediction

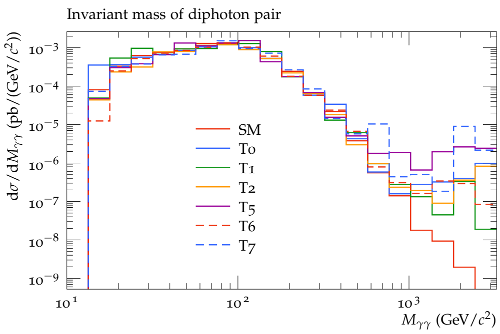

(d) Plot of $m_{\gamma\gamma}$ for full EFT contribution of all T Operators plotted with the SM prediction

Figure 4.4: Plots of the diff. cross section against $m_{\gamma\gamma}$ for EFT operators and different contributions of decomposition

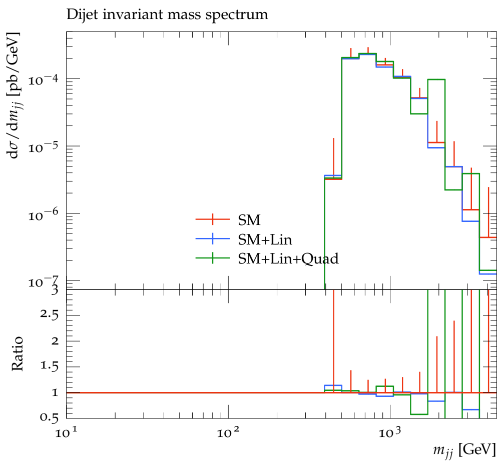

(a) Diff. cross section against m_{jj} for $\mathcal{L}_{M1}$

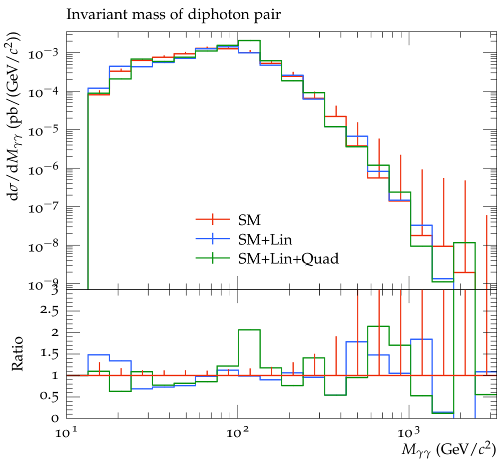

(b) Diff. cross section against $m_{\gamma\gamma}$ for $\mathcal{L}_{M1}$

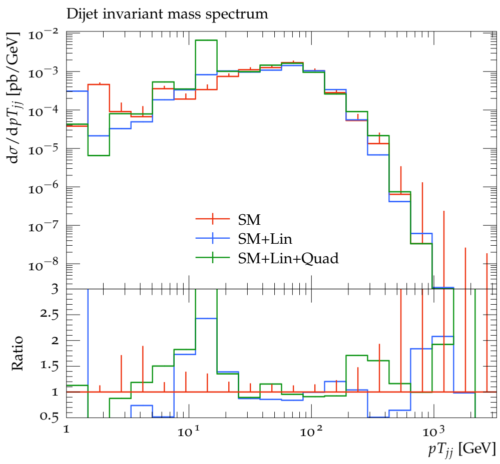

(c) Diff. cross section against $p_{T_{jj}}$ for $\mathcal{L}_{M1}$

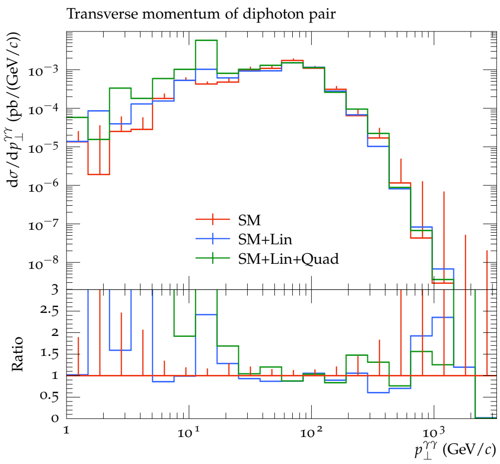

(d) Diff. cross section against $p_{T_{\gamma\gamma}}$ for $\mathcal{L}_{M1}$

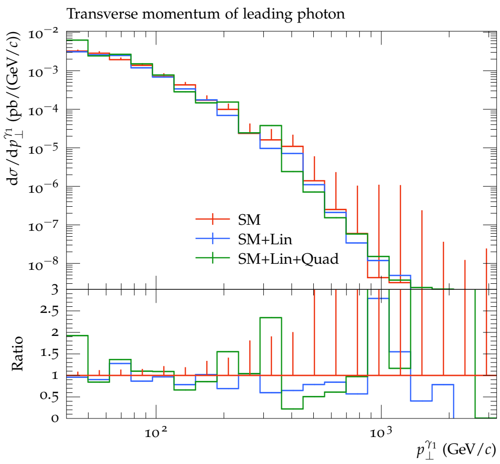

(e) Diff. cross section against $p_{T_{\gamma 1}}$ for $\mathcal{L}_{M1}$

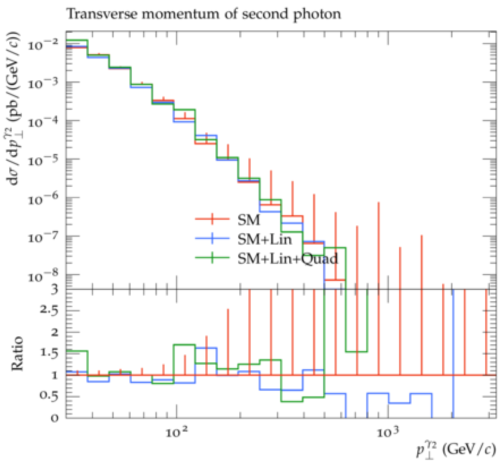

(f) Diff. cross section against $p_{T_{\gamma 2}}$ for $\mathcal{L}_{M1}$

Figure 4.5: Effects of $\mathcal{L}_{M1}$ on the diff. cross section for different variables and SM diff. cross section with statistical and systematic uncertainties.

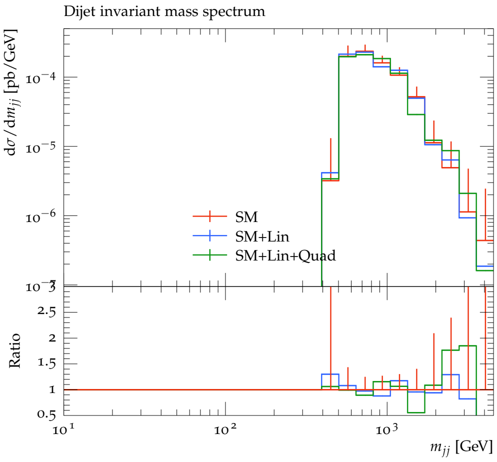

(a) Diff. cross section against m_{jj} for $\mathcal{L}_{M2}$

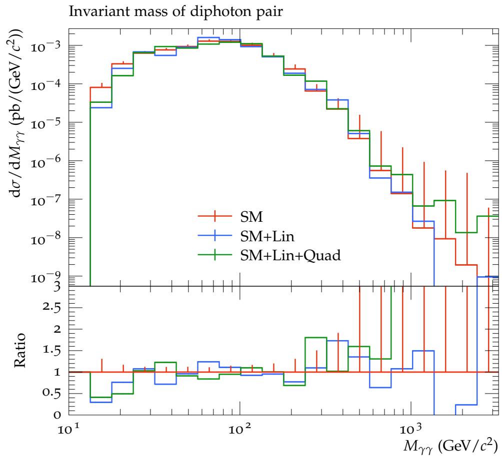

(b) Diff. cross section against $m_{\gamma\gamma}$ for $\mathcal{L}_{M2}$

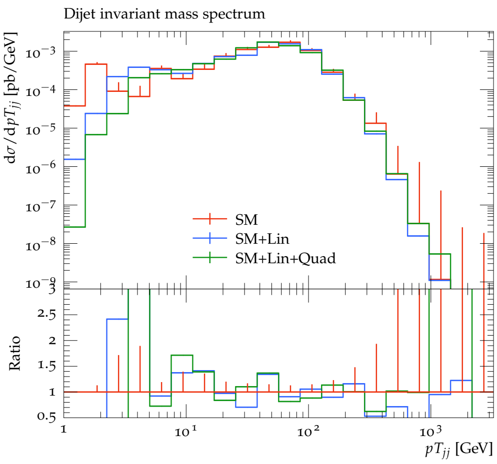

(c) Diff. cross section against $p_{T_{jj}}$ for $\mathcal{L}_{M2}$

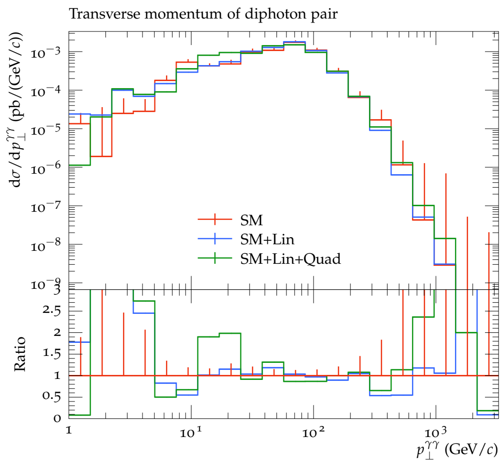

(d) Diff. cross section against $p_{T_{\gamma\gamma}}$ for $\mathcal{L}_{M2}$

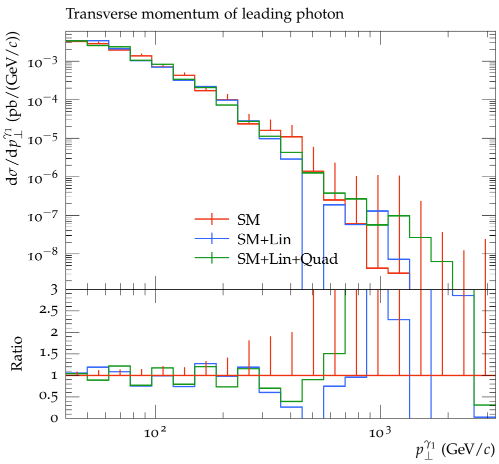

(e) Diff. cross section against $p_{T_{\gamma 1}}$ for $\mathcal{L}_{M2}$

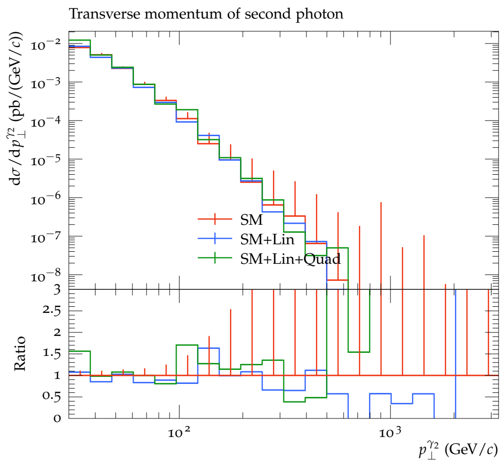

(f) Diff. cross section against $p_{T_{\gamma 2}}$ for $\mathcal{L}_{M2}$

Figure 4.6: Effects of $\mathcal{L}_{M2}$ on the diff. cross section for different variables and SM diff. cross section with statistical and systematic uncertainties.

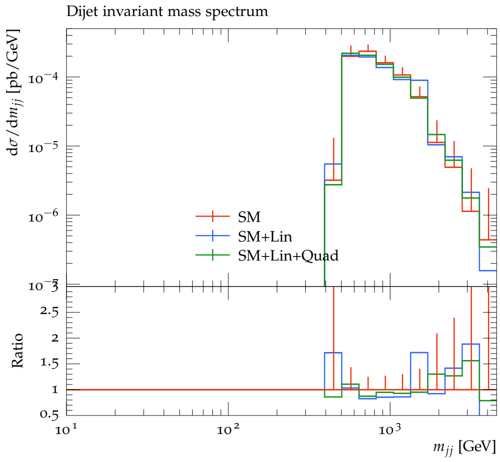

(a) Diff. cross section against m_{jj} for $\mathcal{L}_{T0}$

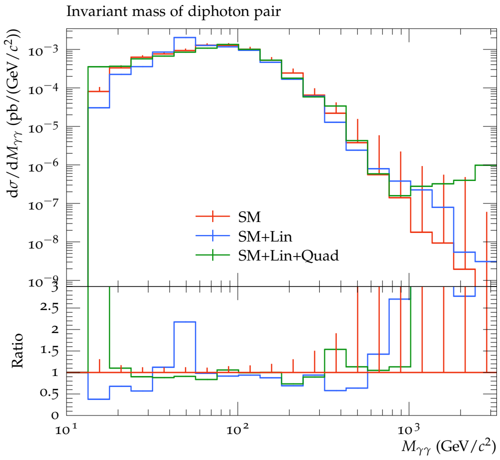

(b) Diff. cross section against $m_{\gamma\gamma}$ for $\mathcal{L}_{T0}$

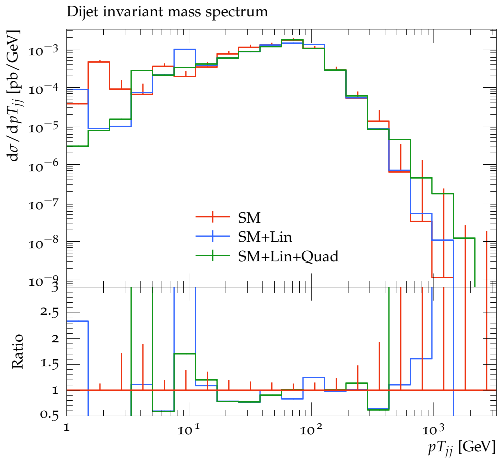

(c) Diff. cross section against $p_{T_{jj}}$ for $\mathcal{L}_{T0}$

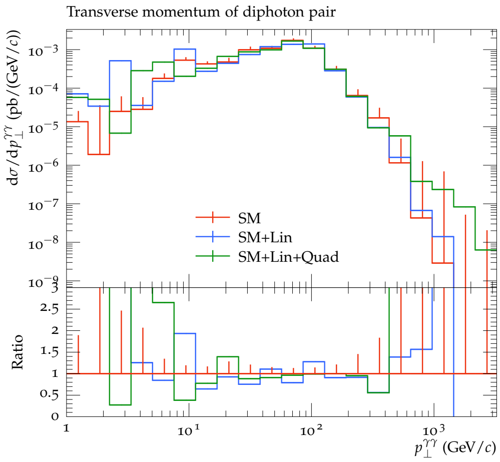

(d) Diff. cross section against $p_{T_{\gamma\gamma}}$ for $\mathcal{L}_{T0}$

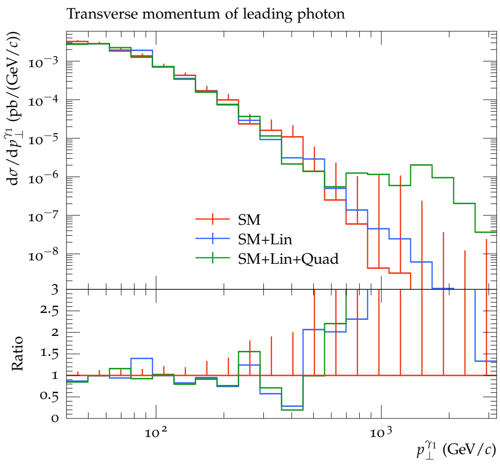

(e) Diff. cross section against $p_{T_{\gamma 1}}$ for $\mathcal{L}_{T0}$

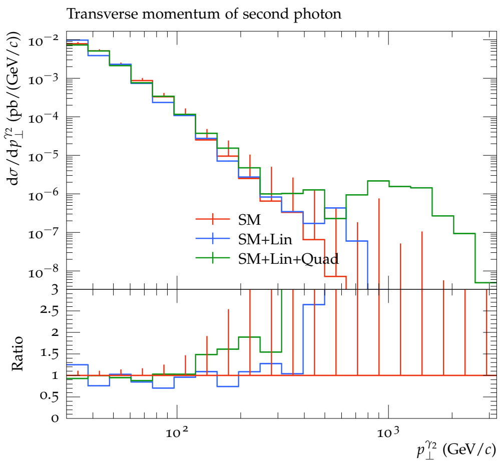

(f) Diff. cross section against $p_{T_{\gamma 2}}$ for $\mathcal{L}_{T0}$

Figure 4.7: Effects of $\mathcal{L}_{T0}$ on the diff. cross section for different variables and SM diff. cross section with statistical and systematic uncertainties.

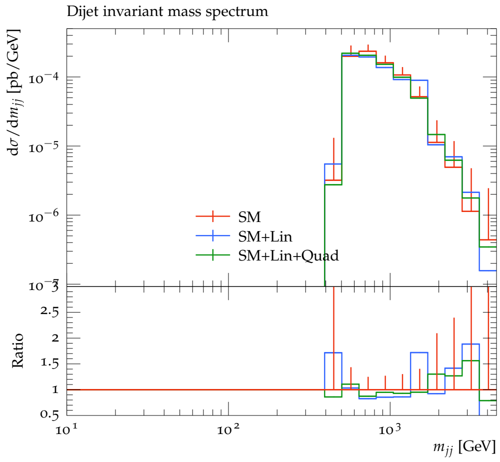

(a) Diff. cross section against m_{jj} for $\mathcal{L}_{T5}$

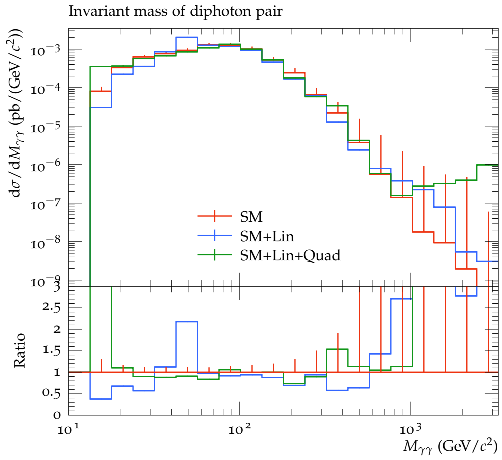

(b) Diff. cross section against $m_{\gamma\gamma}$ for $\mathcal{L}_{T5}$

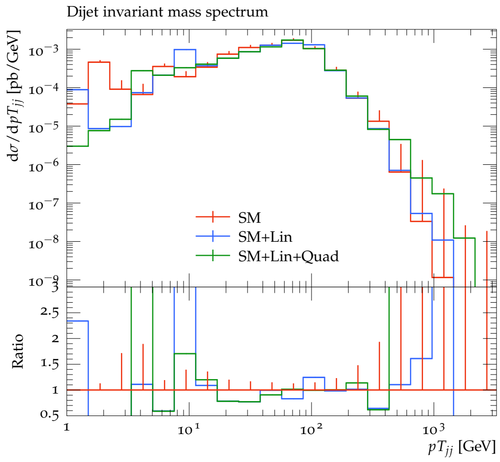

(c) Diff. cross section against $p_{T_{jj}}$ for $\mathcal{L}_{T5}$

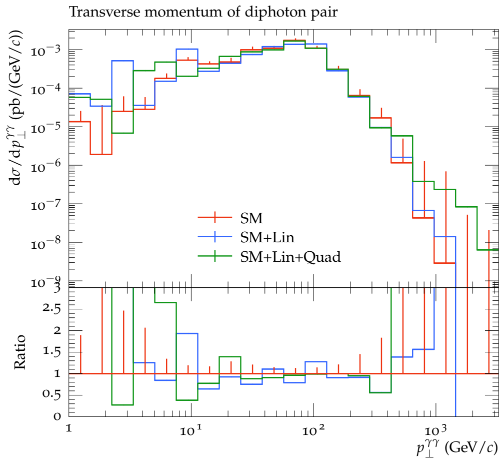

(d) Diff. cross section against $p_{T_{\gamma\gamma}}$ for $\mathcal{L}_{T5}$

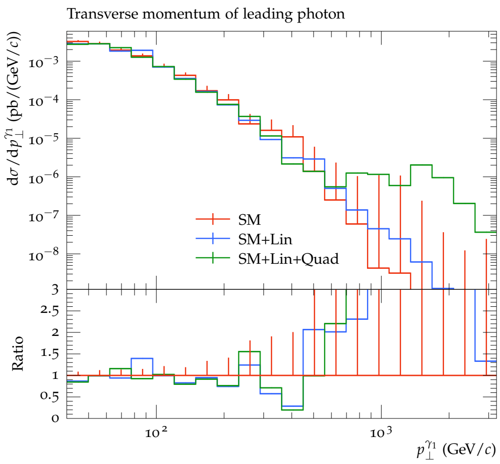

(e) Diff. cross section against $p_{T_{\gamma 1}}$ for $\mathcal{L}_{T5}$

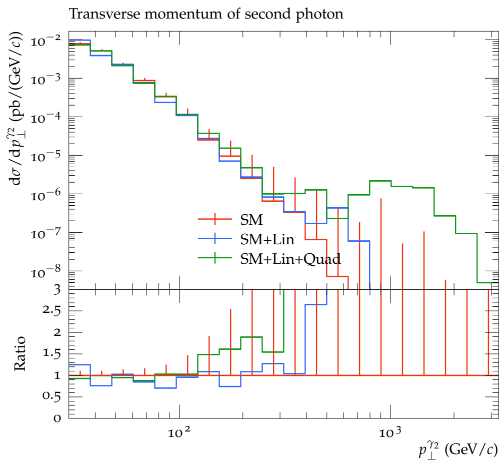

(f) Diff. cross section against $\Delta\phi_{\gamma 2}$ for $\mathcal{L}_{T5}$

Figure 4.8: Effects of $\mathcal{L}_{T5}$ on the diff. cross section for different variables and SM diff. cross section with statistical and systematic uncertainties.

5 Summary and Outlook

The goal of this thesis was to compare the differential cross sections predicted by the SM to those obtained by extending the SM with dim-8 EFT operators. This was done to see if improvements to the current limits of the Wilson coefficients of the EFT operators could be possible with the current technical limitations in center of mass energy and integrated luminosity of the LHC. For the M operators some deviations from the SM predictions could be found in the data, for the operators containing the $B^{\mu\nu}$ field. However these deviations are probably not large enough to allow for improvements of the EFT limits as they were within the SM uncertainties. The T operators on the other hand leave more room for improvements since they seem to be more sensitive to the di-photon production process. The deviations observed in the transverse momenta of the photons are clearly outside of the SM uncertainties, although to confirm that the deviations truly are large enough it would be necessary to analyze the uncertainties more thoroughly, and more events would have to be generated in order to reduce any effects introduced by the MC simulation.

For an actual improvement of the EFT limits, it would first be necessary to find the reason for the deviations between the SM events generated with and without the EFT model. In this thesis a few possibilities as for example slight changes in the SHERPA runcard settings were considered as the reason for this, but none of those were found to be the reason. A possibility which could not be tested is that the EFT model does not correctly apply the QCD order, which would lead to the EW signal also containing the QCD background. For this the QCD background generated with and without the EFT model would need to be compared. If they do not deviate, that could be a hint, that this might be the cause of the issue. Unfortunately due to the limitations of the time-frame for this thesis, it was not possible to test this hypothesis. Another possibility is that the implementation of the EFT model into SHERPA does not work as intended. This could be either because the "Sherpa-generate-model" script, which adds the EFT model to SHERPA, does not function properly or because the EFT model, which was originally created for the use in MadGraph, is not optimized for the use within SHERPA and would have to be adjusted. Regardless of what the problem is exactly, it would have to be fixed to be able to use the results from this thesis for future studies.

If the observed effects turn out to be correct, then in future works some additional steps would have to be taken to confirm the observations and actually improve the limits. These steps would involve generating a higher number of events to minimize the uncertainties added by the MC generation and also to consider more systematic uncertainties for e.g. the normalization. Also considering diagrams at NLO could improve the measurements and would reduce new systematic uncertainties and those already considered. For the QCD productions, considering NLO diagrams could already decrease the renormalization scale correction from $\sim 30\%$ to $\sim 20\%$ [39]. It could also be necessary to study the effects of dim-12 EFT operators on this vertex, since the linear contributions of those are of the same order as the quadratic contributions of the dim-8 EFT operators (Λ^{-4}). Finally it would be necessary to compare the simulated data to actual data from the ATLAS detector to confirm the simulated data does correspond to reality.

A definite way of improving the limits would be to have higher beam energies, and to look at data with higher integrated luminosity. This would decrease the relative statistical uncertainties, since it would increase the number of events counted in each bin. However, for simulated data to be comparable with experimental data of that kind, run 3 of the LHC has to be completed and the data has to be analyzed. Only then would it be possible to compare simulations containing these improvements with real data.

Bibliography

[1] Enrico Bothmann et al. „Event generation with Sherpa 2.2". In: *SciPost Physics* 7.3 (Sept. 2019). ISSN: 2542-4653. DOI: 10.21468/scipostphys.7.3.034. URL: http://dx.doi.org/10.21468/SciPostPhys.7.3.034.

[2] Atlas Collaboration. „Observation and Cross Section Measurements of 3 Electroweak $W(\rightarrow l\nu)\gamma jj$ in Proton-Proton collisions at $\sqrt{s} = 13$ TeV with the ATLAS Detector". In: (2023). (Work in progress). URL: https://cds.cern.ch/record/2819968.

[3] Oliver Sim Brüning et al. *LHC Design Report*. CERN Yellow Reports: Monographs. Geneva: CERN, 2004. DOI: 10.5170/CERN-2004-003-V-1. URL: https://cds.cern.ch/record/782076.

[4] *Technical Design Report for the Phase-II Upgrade of the ATLAS TDAQ System*. Tech. rep. Geneva: CERN, 2017. DOI: 10.17181/CERN.2LBB.4IAL. URL: https://cds.cern.ch/record/2285584.

[5] CERN. *The Large Hadron Collider*. (last visited 02.11.2023). URL: https://home.web.cern.ch/science/accelerators/large-hadron-collider.

[6] The ATLAS collaboration. „Observation of a new particle in the search for the Standard Model Higgs boson with the ATLAS detector at the LHC". In: *Physics Letters B* 716.1 (Sept. 2012), 1–29. ISSN: 0370-2693. DOI: 10.1016/j.physletb.2012.08.020. URL: http://dx.doi.org/10.1016/j.physletb.2012.08.020.

[7] *Luminosity determination in pp collisions at $\sqrt{s} = 13$ TeV using the ATLAS detector at the LHC*. Tech. rep. All figures including auxiliary figures are available at https://atlas.web.cern.ch/ CONF-2019-021. Geneva: CERN, 2019. URL: https://cds.cern.ch/record/2677054.

[8] The ATLAS Collaboration. „The ATLAS Experiment at the CERN Large Hadron Collider". In: *Journal of Instrumentation* 3.08 (2008), S08003. DOI: 10.1088/1748-0221/3/08/S08003. URL: https://dx.doi.org/10.1088/1748-0221/3/08/S08003.

[9] *Das ATLAS Experiment*. (last visited 17.01.2024. URL: https://www.mpg.de/418074/forschungsSchwerpunkt1.

[10] Karl Jakobs. *ATLAS - der Detektor*. (last visited 02.11.2023). URL: https://www.weltderphysik.de/gebiet/teilchen/experimente/teilchenbeschleuniger/cern-lhc/lhc-experimente/atlas/atlas-detektor/.

[11] Guido ALTARELLI. *The Standard Model of Particle Physics*. 2005. arXiv: hep-ph/0510281 [hep-ph].

[12] Mark Thomson. *Modern particle physics*. New York: Cambridge University Press, 2013. ISBN: 978-1-107-03426-6. DOI: 10.1017/CBO9781139525367.

[13] Markus Q. Huber. *Nonperturbative properties of Yang-Mills theories*. 2020. arXiv: 1808.05227 [hep-ph].

[14] (last visited 23.12.2023). URL: https://upload.wikimedia.org/wikipedia/commons/0/00/Standard_Model_of_Elementary_Particles.svg.

[15] Martin F. Sohnius. „Introducing supersymmetry“. In: *Physics Reports* 128.2 (1985), pp. 39–204. ISSN: 0370-1573. DOI: https://doi.org/10.1016/0370-1573(85)90023-7. URL: https://www.sciencedirect.com/science/article/pii/0370157385900237.

[16] Stephan Narison. *QCD as a Theory of Hadrons: From Partons to Confinement*. Cambridge Monographs on Particle Physics, Nuclear Physics and Cosmology. Cambridge University Press, 2004. DOI: 10.1017/CBO9780511535000.

[17] Peter W. Higgs. „Broken Symmetries and the Masses of Gauge Bosons“. In: *Phys. Rev. Lett.* 13 (16 1964). DOI: 10.1103/PhysRevLett.13.508. URL: https://link.aps.org/doi/10.1103/PhysRevLett.13.508.

[18] F. Englert and R. Brout. „Broken Symmetry and the Mass of Gauge Vector Mesons“. In: *Phys. Rev. Lett.* 13 (9 1964). DOI: 10.1103/PhysRevLett.13.321. URL: https://link.aps.org/doi/10.1103/PhysRevLett.13.321.

[19] G. S. Guralnik, C. R. Hagen, and T. W. B. Kibble. „Global Conservation Laws and Massless Particles“. In: *Phys. Rev. Lett.* 13 (20 1964). DOI: 10.1103/PhysRevLett.13.585. URL: https://link.aps.org/doi/10.1103/PhysRevLett.13.585.

[20] Antonio Pich. *The Standard Model of Electroweak Interactions*. 2012. arXiv: 1201.0537 [hep-ph].

[21] *Solving a mystery.* (last visited 02.11.2023). URL: https://muon-g-2.fnal.gov/muon-g-2-collaboration-to-solve-mystery.html.

[22] Stefanie Todt. „The $W^\pm W^\pm$ Scattering Process – Theoretical Studies, Observation, Cross-section Measurement, and EFT Reinterpretation at $\sqrt{s} = 13$ TeV with the ATLAS Detector“. Presented 02 Dec 2022. TU Dresden, 2022. URL: https://cds.cern.ch/record/2845282.

[23] Raquel Gomez-Ambrosio. „Studies of Gauge Couplings at LHC: the Effective Field Theory Approach“. In: (Oct. 2017). DOI: 10.13140/RG.2.2.23472.87049.

[24] Fred L. Wilson. „Fermi's Theory of Beta Decay". In: *American Journal of Physics* 36.12 (Dec. 1968), pp. 1150–1160. ISSN: 0002-9505. DOI: 10.1119/1.1974382. eprint: https://pubs.aip.org/aapt/ajp/article-pdf/36/12/1150/11891052/1150_1_online.pdf. URL: https://doi.org/10.1119/1.1974382.

[25] W. Buchmüller and D. Wyler. „Effective lagrangian analysis of new interactions and flavour conservation". In: *Nuclear Physics B* 268.3 (1986), pp. 621–653. ISSN: 0550-3213. DOI: https://doi.org/10.1016/0550-3213(86)90262-2. URL: https://www.sciencedirect.com/science/article/pii/0550321386902622.

[26] Brian Henning et al. *2, 84, 30, 993, 560, 15456, 11962, 261485, ...: Higher dimension operators in the SM EFT*. 2019. arXiv: 1512.03433 [hep-ph]. URL: https://arxiv.org/abs/1512.03433.

[27] O.J.P. Éboli M.C. Gonzalez–Garcia. *Anomalous quartic electroweak gauge-boson interactions*. (last visited 26.10.2023). 2012. URL: https://feynrules.irmp.ucl.ac.be/wiki/AnomalousGaugeCoupling#no1.

[28] O.J.P. Éboli M.C. Gonzalez–Garcia. *Classifying the bosonic quartic couplings*. 2016. URL: https://journals.aps.org/prd/pdf/10.1103/PhysRevD.93.093013.

[29] O.J.P. Éboli and M.C. Gonzalez–Garcia. „Classifying the bosonic quartic couplings". In: *Physical Review D* 93.9 (May 2016). ISSN: 2470-0029. DOI: 10.1103/physrevd.93.093013. URL: http://dx.doi.org/10.1103/PhysRevD.93.093013.

[30] T Gleisberg et al. „Event generation with SHERPA 1.1". In: *Journal of High Energy Physics* 2009.02 (Feb. 2009), 007–007. ISSN: 1029-8479. DOI: 10.1088/1126-6708/2009/02/007. URL: http://dx.doi.org/10.1088/1126-6708/2009/02/007.

[31] Tanju Gleisberg and Stefan Höche. „Comix, a new matrix element generator". In: *Journal of High Energy Physics* 2008.12 (Dec. 2008), 039–039. ISSN: 1029-8479. DOI: 10.1088/1126-6708/2008/12/039. URL: http://dx.doi.org/10.1088/1126-6708/2008/12/039.

[32] *Sherpa Manual*. (last visited 18.01.2024). URL: https://sherpa-team.gitlab.io/sherpa/v3.0.0beta1/index.html.

[33] Matteo Cacciari, Gavin P. Salam, and Gregory Soyez. „FastJet user manual: (for version 3.0.2)". In: *The European Physical Journal C* 72.3 (Mar. 2012). ISSN: 1434-6052. DOI: 10.1140/epjc/s10052-012-1896-2. URL: http://dx.doi.org/10.1140/epjc/s10052-012-1896-2.

[34] Matteo Cacciari, Gavin P Salam, and Gregory Soyez. „The anti-ktjet clustering algorithm". In: *Journal of High Energy Physics* 2008.04 (Apr. 2008), 063–063. ISSN: 1029-8479. DOI: 10.1088/1126-6708/2008/04/063. URL: http://dx.doi.org/10.1088/1126-6708/2008/04/063.

[35] R H Kleiss, William James Stirling, and S D Ellis. „A new Monte Carlo treatment of multiparticle phase space at high energies“. In: *Comput. Phys. Commun.* 40 (1986), pp. 359–373. DOI: 10.1016/0010-4655(86)90119-0. URL: https://cds.cern.ch/record/164736.

[36] Christian Bierlich et al. „Robust Independent Validation of Experiment and Theory: Rivet version 3“. In: *SciPost Physics* 8.2 (Feb. 2020). ISSN: 2542-4653. DOI: 10.21468/scipostphys.8.2.026. URL: http://dx.doi.org/10.21468/SciPostPhys.8.2.026.

[37] *Rivet — the particle-physics MC analysis toolkit.* (last visited 19.12.2023). URL: https://rivet.hepforge.org/.

[38] Shalu Solomon. *Electroweak Vector Boson Scattering Measurements at the LHC.* Tech. rep. Geneva: CERN, 2023. URL: https://cds.cern.ch/record/2853598.

[39] Simon Badger, Alberto Guffanti, and Valery Yundin. „Next-to-leading order QCD corrections to di-photon production in association with up to three jets at the Large Hadron Collider“. In: *Journal of High Energy Physics* 2014.3 (Mar. 2014). ISSN: 1029-8479. DOI: 10.1007/jhep03(2014)122. URL: http://dx.doi.org/10.1007/JHEP03(2014)122.

Selbstständigkeitserklärung

Hiermit versichere ich, dass ich, Justin Gründling, die vorliegende Bachelorarbeit im Rahmen der Betreuung am Institut für Kern- und Teilchenphysik selbstständig verfasst habe und keine anderen als die angegebenen Quellen und Hilfsmittel benutzt sowie Zitate kenntlich gemacht habe.
Diese Arbeit wurde noch nicht in gleicher oder ähnlicher Form im Rahmen einer anderen Prüfungsleistung vorgelegt.

Justin Gründling
Dresden, den 23. Januar 2024

A Appendix

Sherpa runcard example

EW Runcard

```
# general settings
EVENTS: 100000
EVENT_GENERATION_MODE: Weighted
# ME generator setup
ME_GENERATORS: Comix
MEPS:
CORE_SCALE: VARAbs2(p[2]+p[3]);
# other settings
ALPHAQED_DEFAULT_SCALE: 0.0 # variation for alpha_QED
SCALE_VARIATIONS: 4.0* # 7-point scale variation
PSI_ItMin: 25000 # min number of iterations for ME integration
Integration_Error: 0.05
CSS_CSMODE: 1 # no exchange of color charge between jets
EXLUSIVE_CLUSTER_MODE: 1 # reconstruction of jets asumes only QCD interactions
CDXS_VSOPT: 5
TAGS:
QCUT: 10
#Integrator
INTEGRATOR: Rambo
SCALES: METS{MU_F2}{MU_R2}{MU_Q2}
# model setup
MODEL: SM_Ltotal_Ind5v2020v2_UFO
PARTICLE_DATA:
1: {Massive: false}
2: {Massive: false}
3: {Massive: false}
4: {Massive: false}
5: {Massive: false}
11: {Massive: false}
13: {Massive: false}
15: {Massive: false}
# LHC beam setup:
BEAMS: 2212
BEAM_ENERGIES: 6500
# generate all 2 -> 4 yyjj processes that include max 1 EFT vertex
PROCESSES:
- "93 93 -> 22 22 93 93":
Max_Amplitude_Order: QCD: 0,QED: 4,M0: 1,M1: 0,M2: 0,M3: 0,M4: 0,M5: 0,M6: 0,M7: 0,S0: 0,S1: 0,S2: 0,T0: 0,T1: 0,T2: 0,T3: 0,T4: 0,T5:
0,T6: 0,T7: 0,T8: 0,T9: 0
SELECTORS:
- VariableSelector: # Photon cuts
Variable: PT # Transverse Momentum
Flavs: [22] # Photons
Ranges:
- [20, E_CMS] # ranges for p_T of emitted photons
- [18, E_CMS]
Ordering: [PT_UP]
- FastjetFinder:
Algorithm: antikt # Jet cuts
N: 2
PTMin: 20.0
ETMin: 0.0
DR: 0.4
- [IsolationCut, 22, 0.1, 2, 0.10]
- [DR, 22, 22, 0.2, 1000.0]
UFO_PARAMS: | # wilson coefficients (f_i/Lambda4̂) [(GeV)-̂4]
block anoinputs
4 23.87e-12 # FM0, (only as one example)
```

Plots

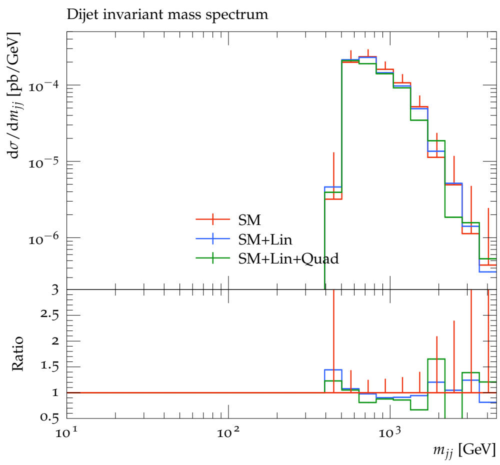

(a) Diff. cross section against m_{jj} for $\mathcal{L}_{M0}$

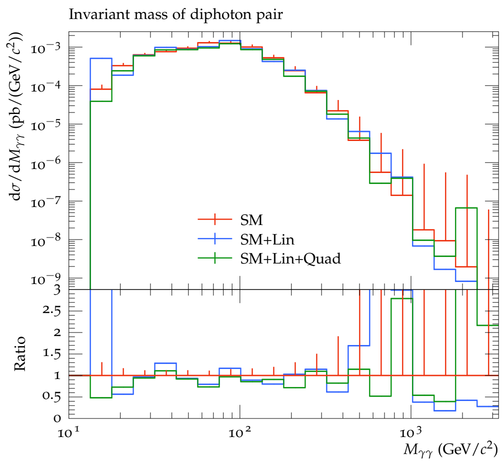

(b) Diff. cross section against $m_{\gamma\gamma}$ for $\mathcal{L}_{M0}$

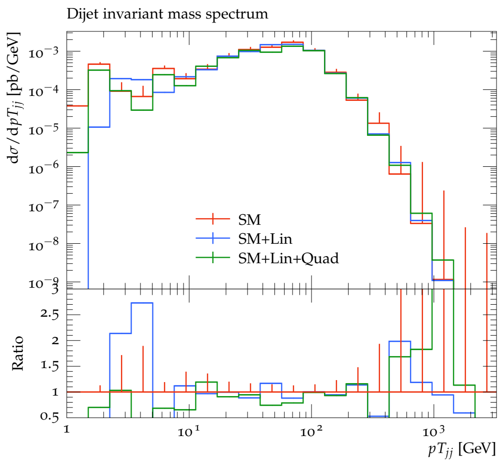

(c) Diff. cross section against $p_{T_{jj}}$ for $\mathcal{L}_{M0}$

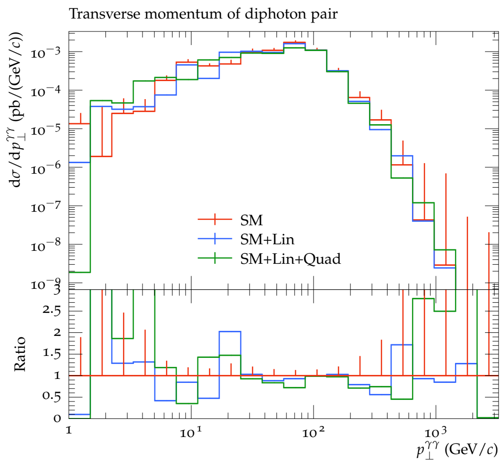

(d) Diff. cross section against $p_{T_{\gamma\gamma}}$ for $\mathcal{L}_{M0}$

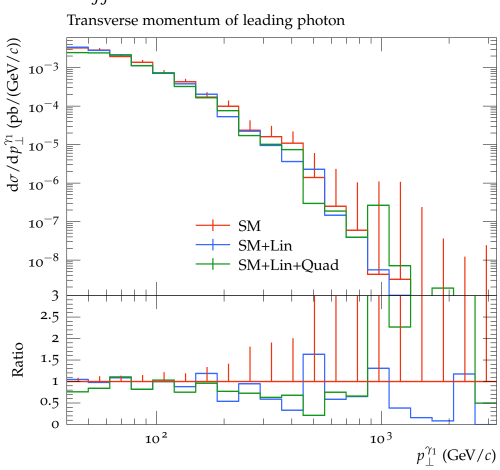

(e) Diff. cross section against $p_{T_{\gamma 1}}$ for $\mathcal{L}_{M0}$

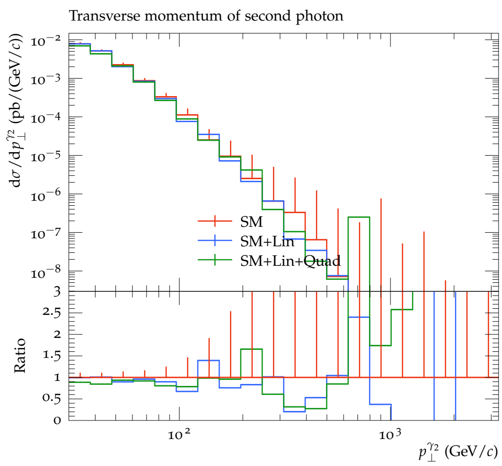

(f) Diff. cross section against $p_{T_{\gamma 2}}$ for $\mathcal{L}_{M0}$

Figure A.1: Effects of $\mathcal{L}_{M0}$ on the diff. cross section for different variables and SM diff. cross section with statistical and systematic uncertainties.

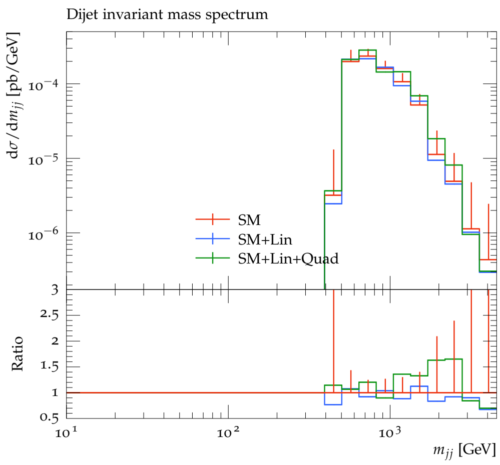

(a) Diff. cross section against m_{jj} for $\mathcal{L}_{M3}$

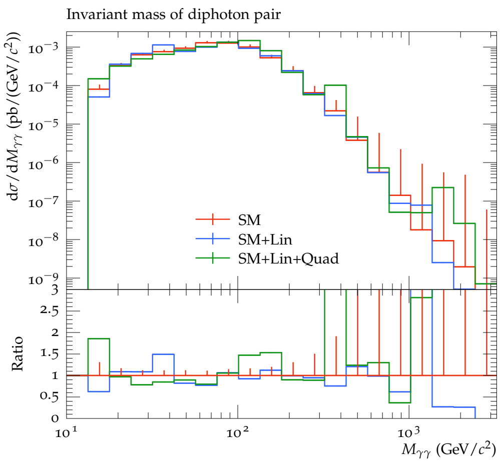

(b) Diff. cross section against $m_{\gamma\gamma}$ for $\mathcal{L}_{M3}$

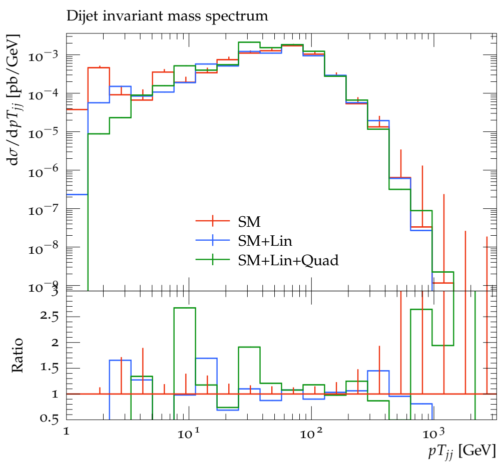

(c) Diff. cross section against $p_{T_{jj}}$ for $\mathcal{L}_{M3}$

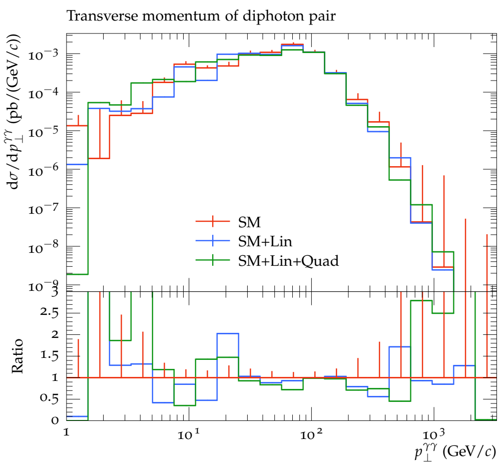

(d) Diff. cross section against $p_{T_{\gamma\gamma}}$ for $\mathcal{L}_{M3}$

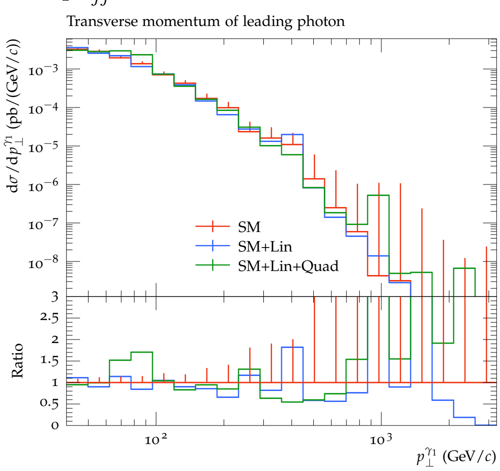

(e) Diff. cross section against $p_{T_{\gamma 1}}$ for $\mathcal{L}_{M3}$

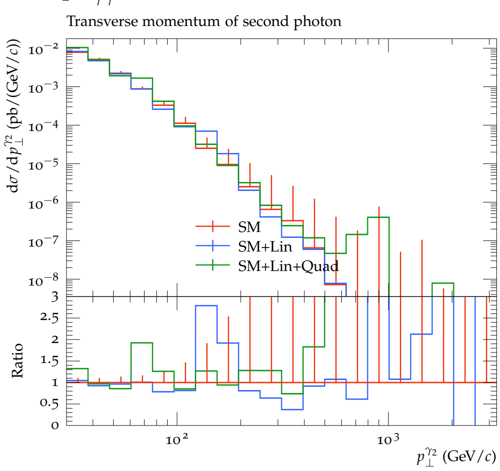

(f) Diff. cross section against $p_{T_{\gamma 2}}$ for $\mathcal{L}_{M3}$

Figure A.2: Effects of $\mathcal{L}_{M3}$ on the diff. cross section for different variables and SM diff. cross section with statistical and systematic uncertainties.

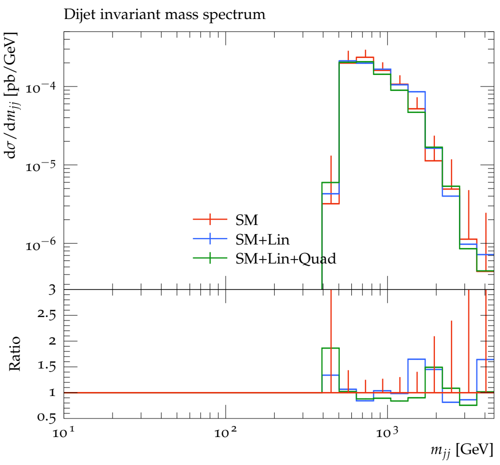

(a) Diff. cross section against m_{jj} for $\mathcal{L}_{M4}$

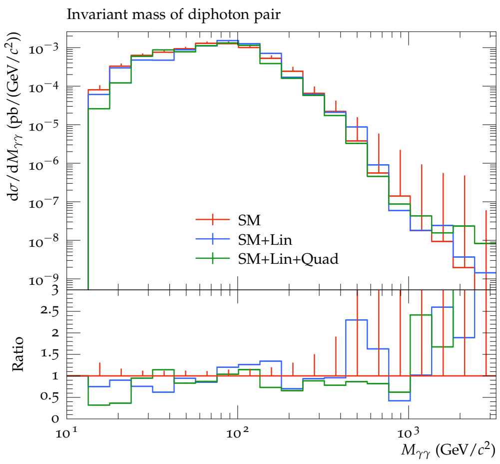

(b) Diff. cross section against $m_{\gamma\gamma}$ for $\mathcal{L}_{M4}$

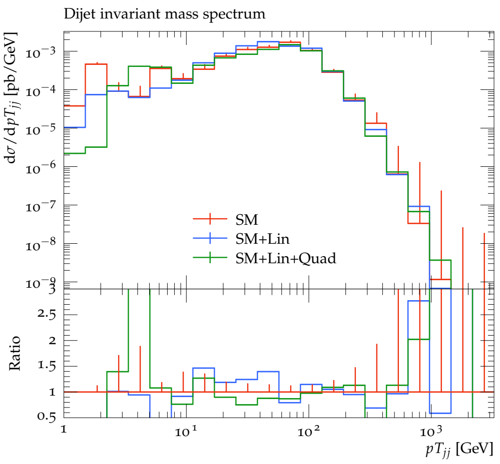

(c) Diff. cross section against $p_{T_{jj}}$ for $\mathcal{L}_{M4}$

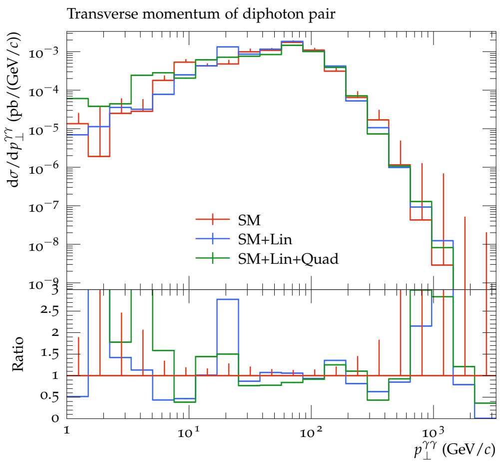

(d) Diff. cross section against $p_{T_{\gamma\gamma}}$ for $\mathcal{L}_{M4}$

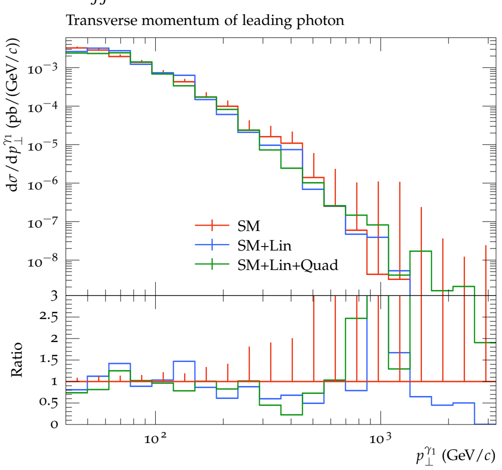

(e) Diff. cross section against $p_{T_{\gamma 1}}$ for $\mathcal{L}_{M4}$

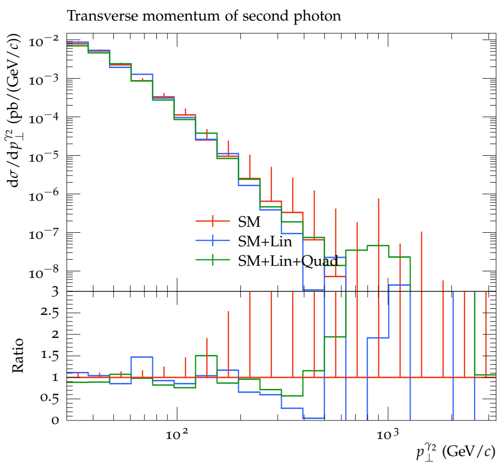

(f) Diff. cross section against $p_{T_{\gamma 2}}$ for $\mathcal{L}_{M4}$

Figure A.3: Effects of $\mathcal{L}_{M4}$ on the diff. cross section for different variables and SM diff. cross section with statistical and systematic uncertainties.

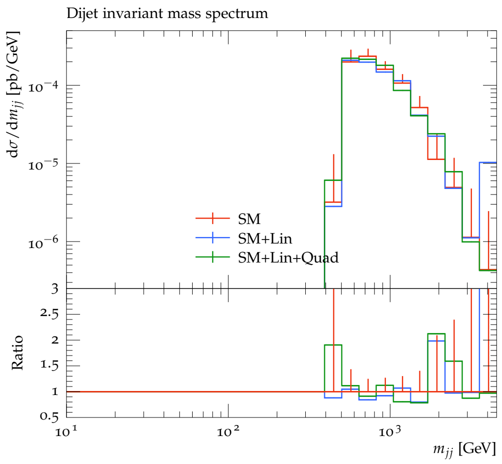

(a) Diff. cross section against m_{jj} for $\mathcal{L}_{M5}$

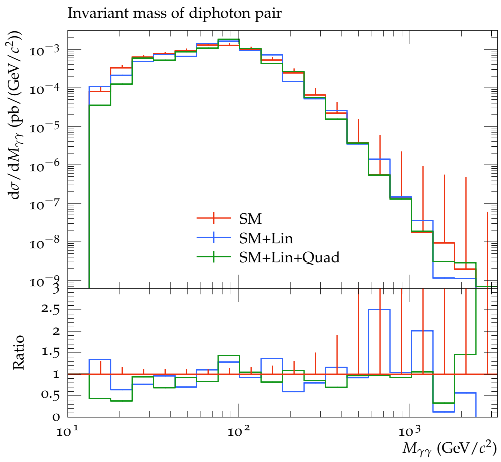

(b) Diff. cross section against $m_{\gamma\gamma}$ for $\mathcal{L}_{M5}$

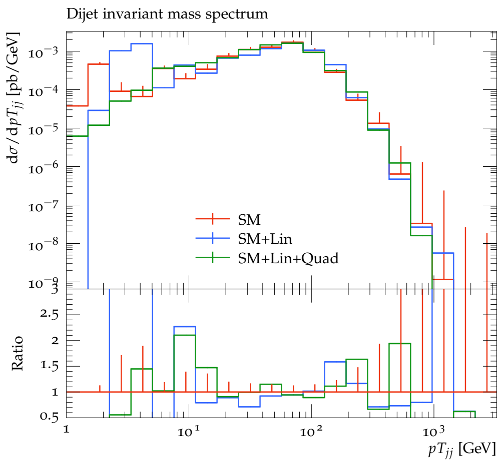

(c) Diff. cross section against $p_{T_{jj}}$ for $\mathcal{L}_{M5}$

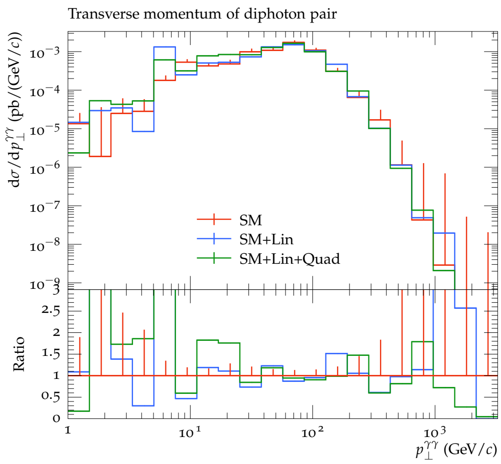

(d) Diff. cross section against $p_{T_{\gamma\gamma}}$ for $\mathcal{L}_{M5}$

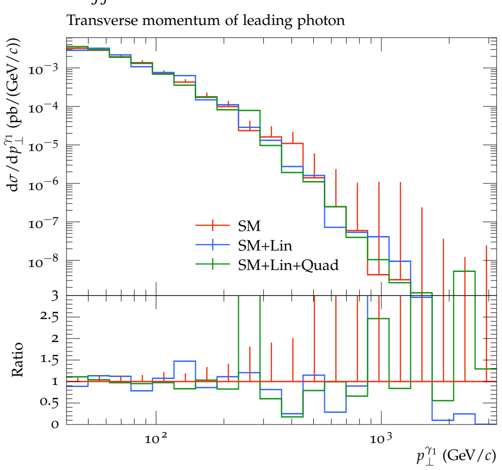

(e) Diff. cross section against $p_{T_{\gamma 1}}$ for $\mathcal{L}_{M5}$

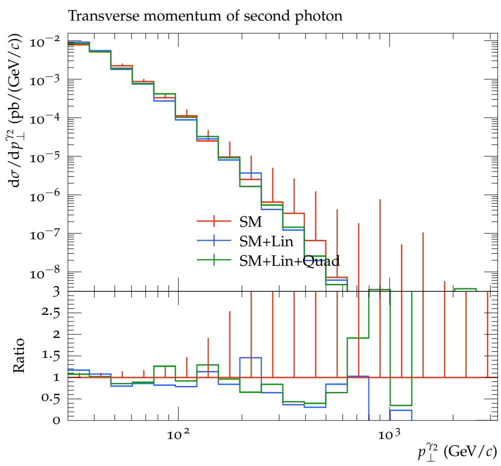

(f) Diff. cross section against $p_{T_{\gamma 2}}$ for $\mathcal{L}_{M5}$

Figure A.4: Effects of $\mathcal{L}_{M5}$ on the diff. cross section for different variables and SM diff. cross section with statistical and systematic uncertainties.

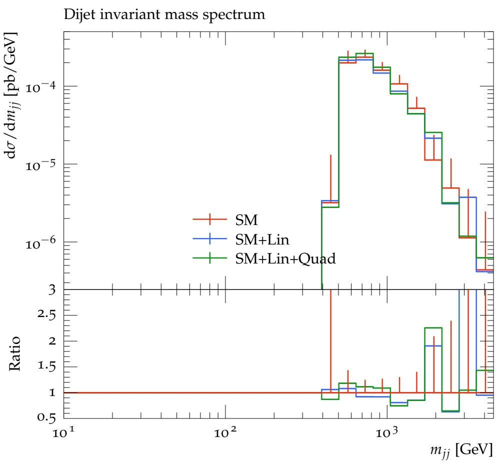

(a) Diff. cross section against m_{jj} for $\mathcal{L}_{M7}$

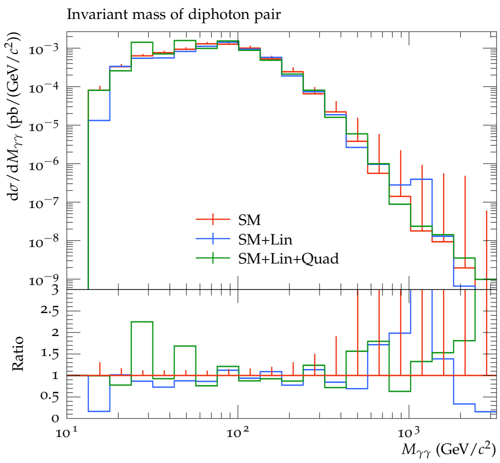

(b) Diff. cross section against $m_{\gamma\gamma}$ for $\mathcal{L}_{M7}$

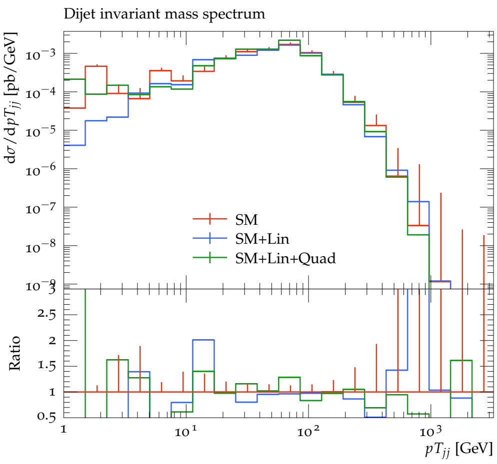

(c) Diff. cross section against $p_{T_{jj}}$ for $\mathcal{L}_{M7}$

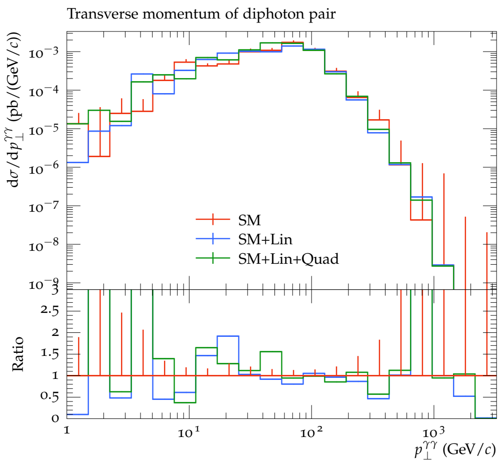

(d) Diff. cross section against $p_{T_{\gamma\gamma}}$ for $\mathcal{L}_{M7}$

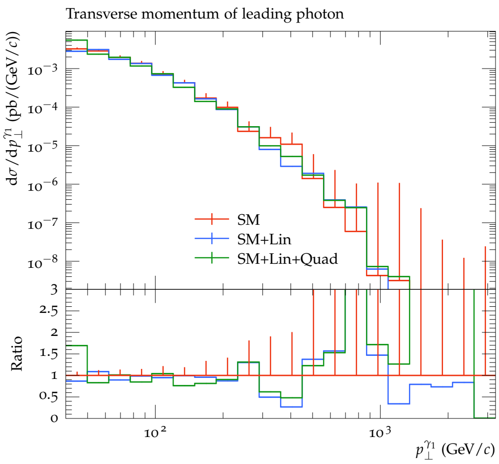

(e) Diff. cross section against $p_{T_{\gamma 1}}$ for $\mathcal{L}_{M7}$

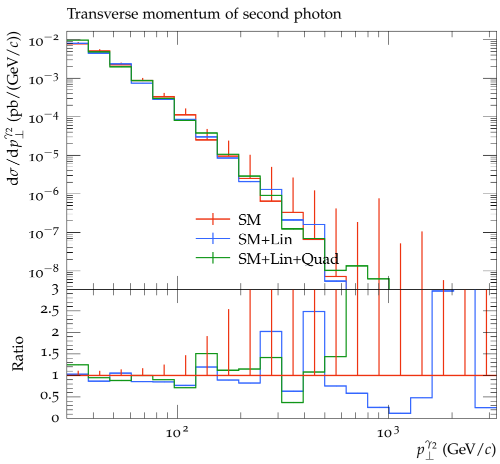

(f) Diff. cross section against $p_{T_{\gamma 2}}$ for $\mathcal{L}_{M7}$

Figure A.5: Effects of $\mathcal{L}_{M7}$ on the diff. cross section for different variables and SM diff. cross section with statistical and systematic uncertainties.

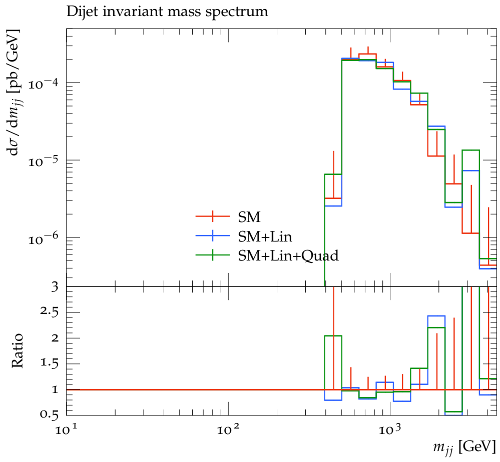

(a) Diff. cross section against m_{jj} for $\mathcal{L}_{T1}$

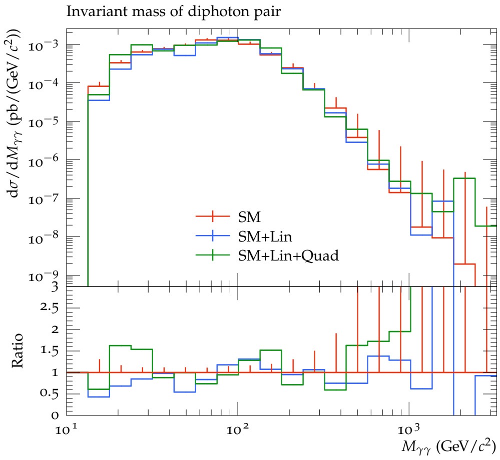

(b) Diff. cross section against $m_{\gamma\gamma}$ for $\mathcal{L}_{T1}$

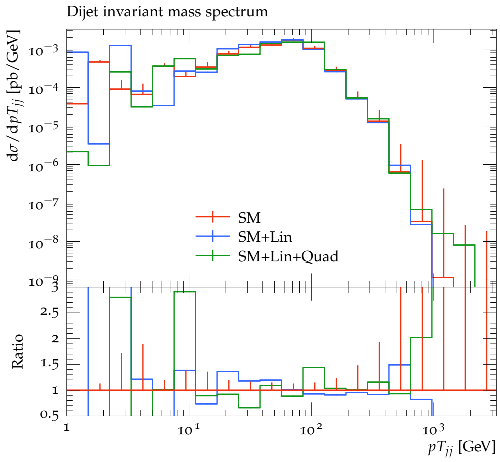

(c) Diff. cross section against $p_{T_{jj}}$ for $\mathcal{L}_{T1}$

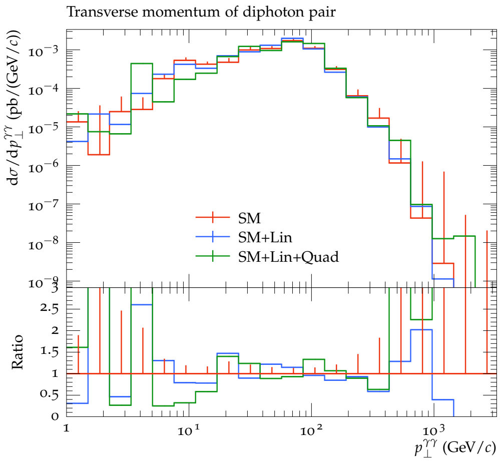

(d) Diff. cross section against $p_{T_{\gamma\gamma}}$ for $\mathcal{L}_{T1}$

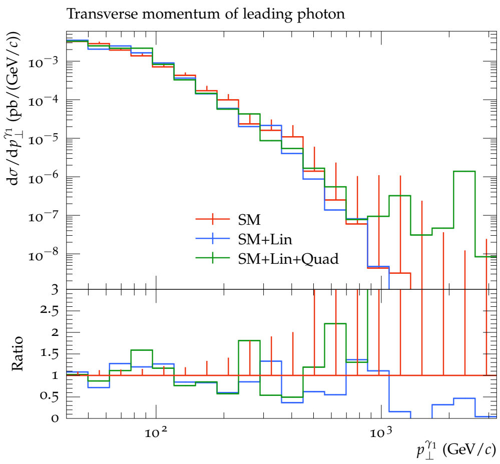

(e) Diff. cross section against $p_{T_{\gamma 1}}$ for $\mathcal{L}_{T1}$

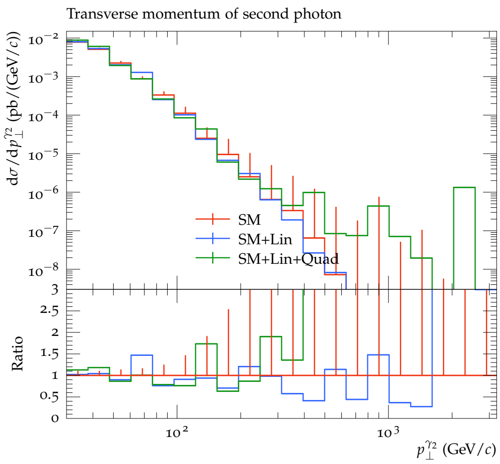

(f) Diff. cross section against $p_{T_{\gamma 2}}$ for $\mathcal{L}_{T1}$

Figure A.6: Effects of $\mathcal{L}_{T1}$ on the diff. cross section for different variables and SM diff. cross section with statistical and systematic uncertainties.

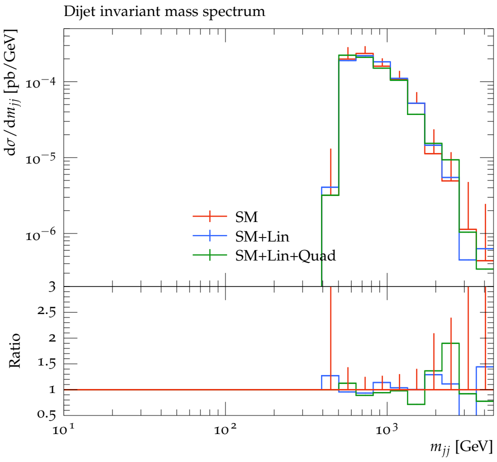

(a) Diff. cross section against m_{jj} for $\mathcal{L}_{T6}$

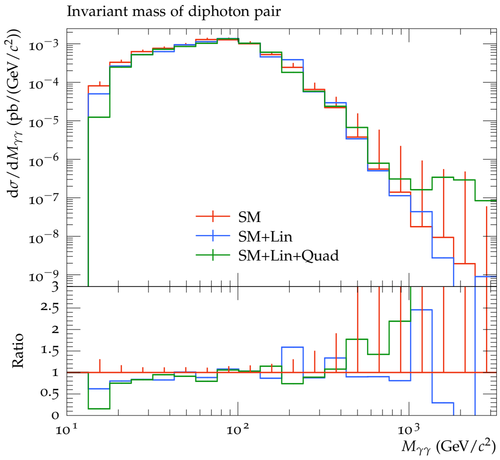

(b) Diff. cross section against $m_{\gamma\gamma}$ for $\mathcal{L}_{T6}$

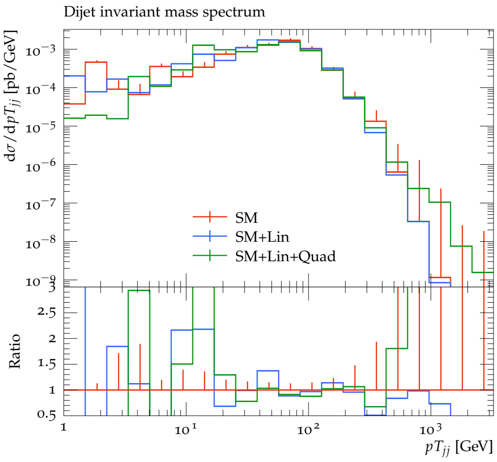

(c) Diff. cross section against $p_{T_{jj}}$ for $\mathcal{L}_{T6}$

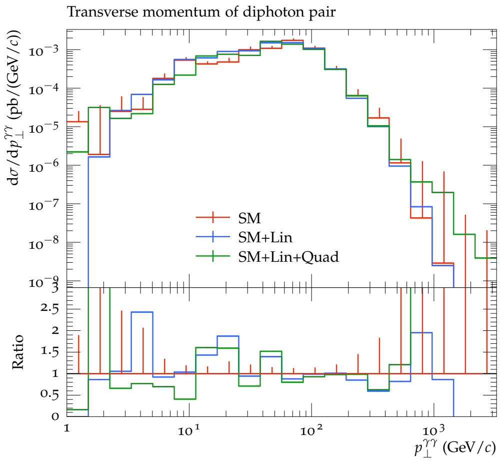

(d) Diff. cross section against $p_{T_{\gamma\gamma}}$ for $\mathcal{L}_{T6}$

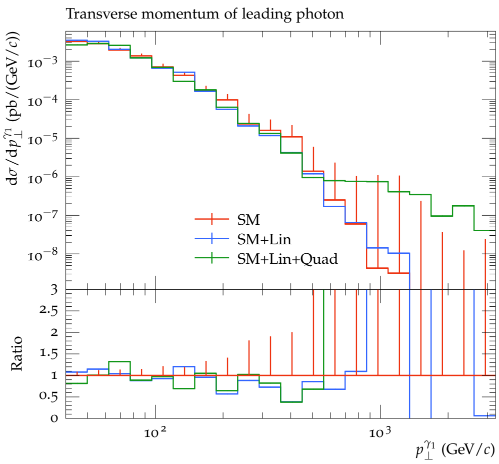

(e) Diff. cross section against $p_{T_{\gamma 1}}$ for $\mathcal{L}_{T6}$

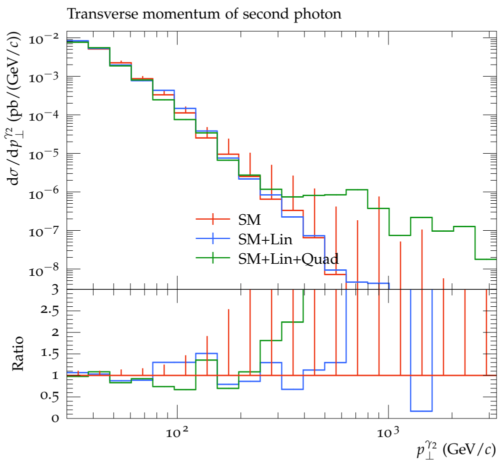

(f) Diff. cross section against $p_{T_{\gamma 2}}$ for $\mathcal{L}_{T6}$

Figure A.7: Effects of $\mathcal{L}_{T6}$ on the diff. cross section for different variables and SM diff. cross section with statistical and systematic uncertainties.

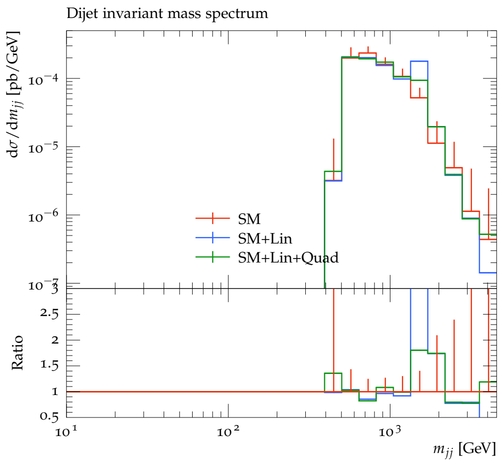

(a) Diff. cross section against m_{jj} for $\mathcal{L}_{T7}$

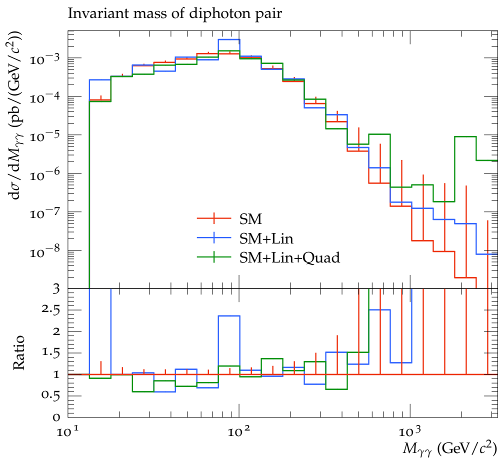

(b) Diff. cross section against $m_{\gamma\gamma}$ for $\mathcal{L}_{T7}$

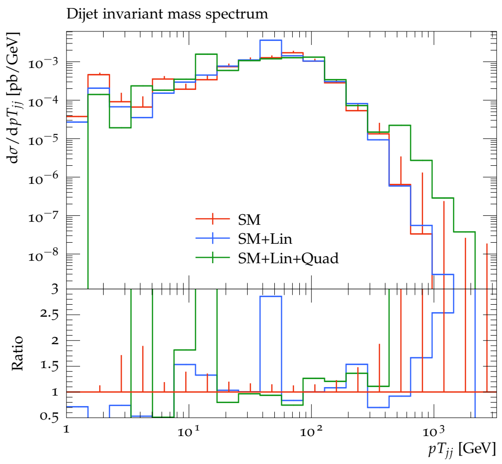

(c) Diff. cross section against $p_{T_{jj}}$ for $\mathcal{L}_{T7}$

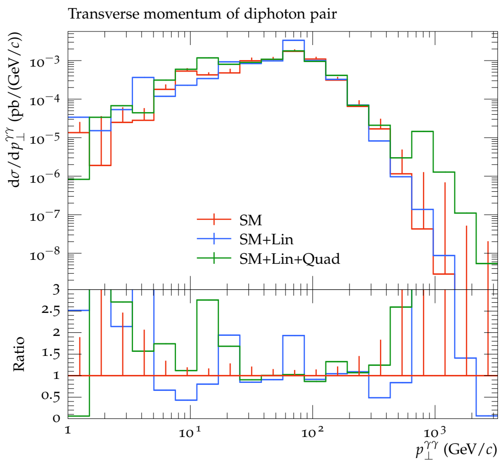

(d) Diff. cross section against $p_{T_{\gamma\gamma}}$ for $\mathcal{L}_{T7}$

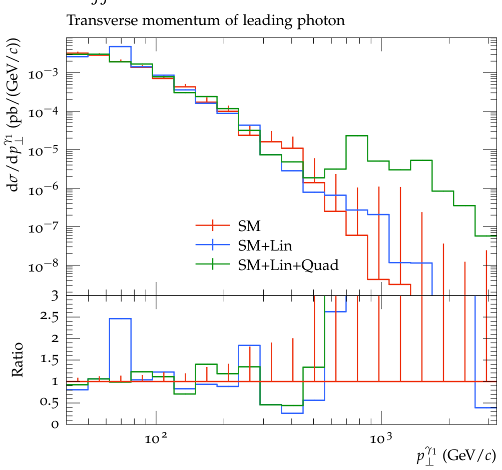

(e) Diff. cross section against $p_{T_{\gamma 1}}$ for $\mathcal{L}_{T7}$

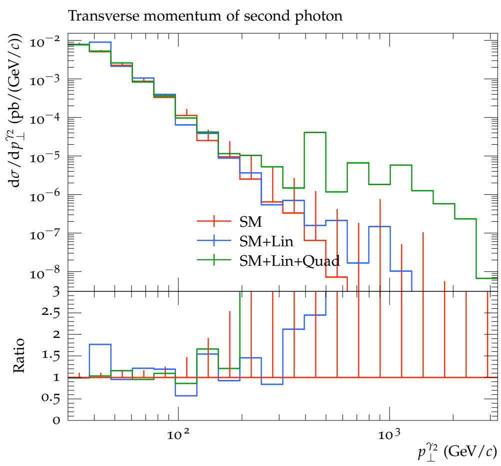

(f) Diff. cross section against $p_{T_{\gamma 2}}$ for $\mathcal{L}_{T7}$

Figure A.8: Effects of $\mathcal{L}_{T7}$ on the diff. cross section for different variables and SM diff. cross section with statistical and systematic uncertainties.